2018-01-01

Effects Of Air And Other Gases In The Stabilization Process Of The Superprotonic Phase Of Cesium Dihydrogen Phosphate Within A Hermetically Sealed Chamber

Israel Martinez
University of Texas at El Paso, rampash@gmail.com

EFFECTS OF AIR AND OTHER GASES IN THE STABILIZATION PROCESS OF THE SUPERPROTONIC PHASE OF CESIUM DIHYDROGEN PHOSPHATE WITHIN A HERMETICALLY SEALED CHAMBER

ISRAEL MARTINEZ VITAL

Doctoral Program in Materials Science and Engineering

APPROVED:

Cristian E. Botez, Ph.D., Chair

Binata Joddar, Ph.D.

Russell R. Chianelli, Ph.D.

Charles Ambler, Ph.D.
Dean of the Graduate School

Dedication

To Dennice, my family and friends.

EFFECTS OF AIR AND OTHER GASES IN THE STABILIZATION PROCESS OF THE SUPERPROTONIC PHASE OF CESIUM DIHYDROGEN PHOSPHATE WITHIN A HERMETICALLY SEALED CHAMBER

by

ISRAEL MARTINEZ VITAL, M.S.

DISSERTATION

Presented to the Faculty of the Graduate School of

The University of Texas at El Paso

in Partial Fulfillment

of the Requirements

for the Degree of

DOCTOR OF PHILOSOPHY

Materials Science and Engineering Program

THE UNIVERSITY OF TEXAS AT EL PASO

August 2018

Acknowledgements

First and foremost, I would like to thank my advisor, Dr. Cristian Botez for all his support during this research project. He guided me in my research and helped me to pursue a higher education. This project was made possible by the support of the grant of the Department of Defense (Grant Number 64705CHREP).

I would also like to acknowledge the Consejo Nacional de Ciencia y Tecnología (CONACyT for its acronym in Spanish) for the scholarship awarded to me. I would also like to thank the members for my defense committee, Dr. Binata Joddar, Dr. Russell Chianelli, for all the help and support and valuable input they've provided me.

And finally, I would like to acknowledge my family, friends, and specially my wife, for all the support and help that provide me through my doctoral studies. Many thanks!

Abstract

The solid acid CsH_2PO_4 (CDP), exhibits a sudden increase in its proton conductivity as it's heated above a certain temperature (around T~235^oC), which makes it a very attractive candidate to be used as an electrolyte in intermediate temperature fuel cells.

Unfortunately, at these temperatures the sample is not stable, as starts to dehydrate; which causes a dramatic drop in the proton conductivity over a short period of time (less than one hour).

In order to inhibit, or at least delay, the dehydration process, the solid acid it's put under a saturated water vapor atmosphere. Another method to stabilize the highly conductive phase is to subject the solid acid to a pressure of ~1GPa. However, none of these methods are practical approaches for making full scale and operational fuel cells.

The main purpose of this research is to find an alternative to stabilize the proton conductivity of CDP at intermediate temperatures, by using hermetically sealed chambers filled with different gases above temperatures of the heated induced high proton conductivity. Also, we mixed CDP with nano-silica $(1-x)CsH_2PO_4 / xSiO_2$ ($0 \leq x \leq 0.3$) for the same purpose. In this study, we used the following characterization techniques: temperature- and time-resolved electrochemical impedance spectroscopy (EIS), x-ray powder diffraction, and thermal analysis methods to analyze the composite $(1-x)CsH_2PO_4 / xSiO_2$ ($0 \leq x \leq 0.3$).

EIS data was collected at different temperatures (200^oC-260^oC) using both, a dry and humid (P_{H_2O} ~ 0.38 atm) atmospheres. EIS was also obtained by using a different volume hermetically sealed chambers filled with Argon, Helium, air, Nitrogen , dry air (with no humidity) and under vacuum.

Table of Contents

List of Tables

List of Figures

List of Illustrations

Chapter 1: Introduction

As the global population grows every year, so does the need to increase energy production. At the beginning of the 19th century almost all the world's energy depended on wood. The first half of the 20th century the production of energy heavily relied on coal, but since then, there has been a shift into oil-based energy production. It's very encouraging that the trend of using oil as the primary source of energy have been decreasing since the begging of the 21st century.

According to analyst at the end of the current century oil will be used primarily in chemical synthesis [1]. Although renewables energy-based technologies have been considered as strong candidates to provide energy (with many experts arguing that specially in rural areas, technologies based on wind, solar or small-scale hydropower can have a huge positive impact)[2], they have so many barriers to overcome (such as market, economic, political, institutional, technical), and sorely relying on them to solve the world's energy demand it's very challenging. Furthermore, a huge obstacle for renewable energy-based creation, it's that they operate in peaks and valleys, making difficult to create a stable production.

Since the middle of the 20th century there has been a lot of effort into transitioning to Hydrogen-based technology for storage and generation of energy which is friendlier to the environment than technologies based on fossil fuel emissions.

Fuel Cells (FCs) are strong candidates as an alternative to fossil fuel, for transportation, and stationary applications [3], [4]. Fuel cells are devices that transform chemical energy into heat and electricity through a catalytic reaction, emitting very low contaminants into the air [5]. Even though we cannot purely rely on hydrogen-based FCs for the generation of energy, they are a step in the right direction as they can be used to storage energy generated from renewable sources like wind, sun or ocean waves [1].

These technologies have advantages over other types of batteries, for instance, lithium batteries present an important loose of its accumulated energy over time, whereas hydrogen-based

FCs can storage energy for longer amount of time, as long as they are continuously supplied with hydrogen and oxygen.

1.1 FUEL CELLS

The most basic design of a fuel cell consists of: an anode, cathode and an electrolyte between them (See illustration 1.1). When a flow of Hydrogen reaches the anode, it becomes ionized, separating its electrons by a catalyst process at the anode. Depending on the technology of the FC, but usually they are coated with precious materials, like platinum, that helps in the catalyst process. The following reaction occurs at the anode:

$$2H_2 \rightarrow 4H^+ + 4e^-$$

A circuit is connected then between the anode and the cathode and the electrons creates an electric current that will be used for the user.

Simultaneously, the protons travel through the electrolyte to the cathode, where Oxygen is supplied creating a reaction with the protons and the electrons arriving from the circuit, producing water and heat.

The reaction at the cathode can be express as:

$$O_2 + 4H^+ + 4e^- \rightarrow 2H_2O$$

In part, is this reaction that makes fuel cells so attractive to be used to storage energy, as the only by-products that they generate its only heat and water. In the 1960's, NASA for the Gemini and Apollo space missions used fuel cells to power the electrical power systems, and the crew drank the water from these fuel cells [6].

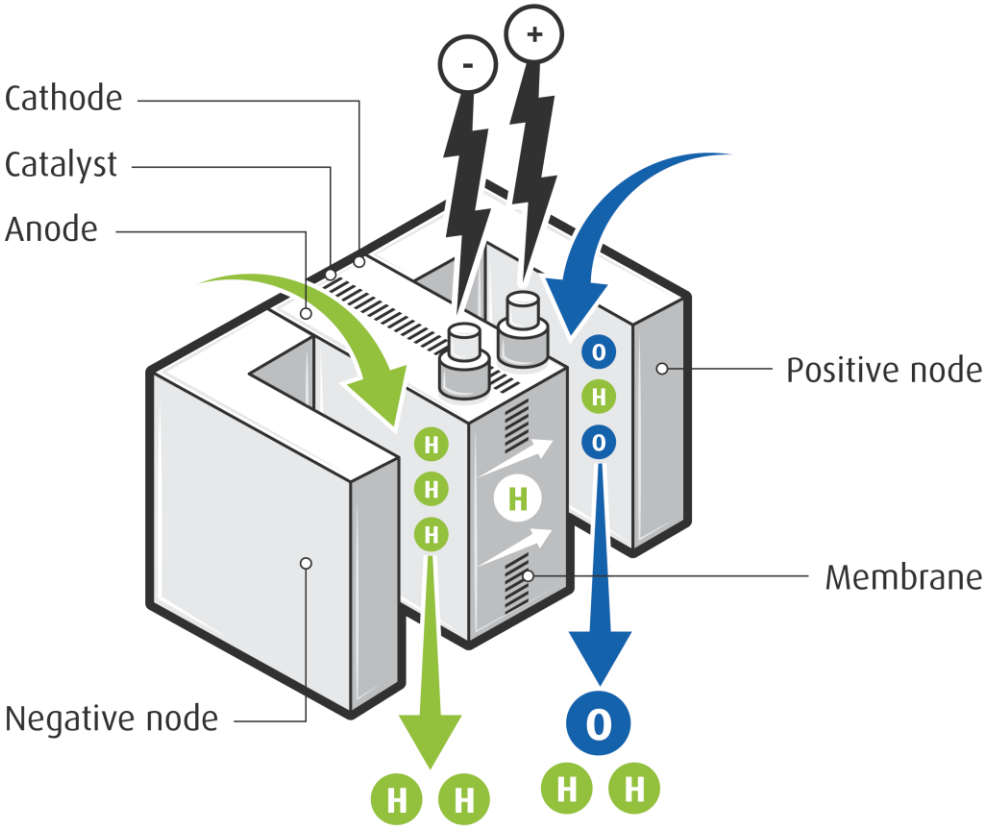

Illustration 1.1 Fuel Cell Basic Components [7]

1.1.1 Types of Fuel Cells

Fuel cells can be classified based on the electrolyte they use and their operational temperature range. Based on the characteristics of each fuel cell we can determine its application. Although there are more types of fuel cells, table 1 presents the most common types of fuel cells.

1.1.1.1 Polymer Electrolyte Membrane Fuel Cells (PEMs)

PEMs tends to have a small size and work at low temperatures (<80°C), this allows them to have a quick start. Since the operational temperature is low, its components wears down at much slower rate than other fuel cells. They uses a solid polymer electrolyte, usually Nafion, with porous carbon electrode and platinum alloys for the catalysis process, which increases manufacturing cost since they use a precious metal. PEMs use Hydrogen as fuel for the anode and oxygen from air to operate. The main application for this type of fuel cell is transportation and stationary applications.

1.1.1.2 Direct Methanol Fuel Cells (DMFCs)

DMFCs uses pure methanol as their fuel, fed directly to the cathode, instead of Hydrogen. Due to its high energy content in a small size, DMFCs have promising use in a variety of portable devices like laptops, cell phones among other others. Though they can produce smaller amount of power through long periods of time, they present operating stability issues. Also, its high manufacturing costs makes a huge drawback for its commercialization. They have a low temperature operation range between 50°C-120°C [8].

1.1.1.3 Alkaline Fuel Cells (AFCs)

AFCs are one of the most mature types of fuel cells, they have been developed since the mid 1960's when NASA used them to power the electrical power systems and provide the crew with a source of drinking water for the Apollo and Space Shuttle programs. This type of devices uses a liquid electrolyte (usually a solution of potassium hydroxide in water, although some polymers are used too) and non-precious materials for the catalytic process, making it a low manufacturing cost.

To avoid damaging the electrolyte, the operating temperature have to reside in the low temperature range (<70°C) and they are very susceptible to CO_2 poisoning in during the catalytic process.

Today's application of the technology is mainly in small off-road vehicles, forklifts and even back-up power for residential homes, hospitals and business.

1.1.1.4 Molten Carbonate Fuel Cells (MCFCs)

MCFCs operates in the high temperature range, in temperatures around 650°C. They use a composite of molten carbonate salt mixture suspended in a lithium aluminum oxide porous matrix. At these elevated temperatures, makes impossible to use precious metals for the catalysis, which decrease the production cost. Methane and other light hydrocarbons are used as fuel.

However, due its extreme operational conditions, the element of the fuel cell wears down a rapid pace, decreasing the life of the fuel cell. The main use of MCFCs are supply industrial, power natural gas and coal-based power plants with electricity.

1.1.1.5 Solid Oxide Fuel Cells (SOFCs)

Since SOFCs can operate a very high temperatures (up to 1000°C), therefore, they don't use precious metals as catalyzers and are very resistant for sulfur or carbon monoxide poisoning.

They use natural gas, biomass, and even gases from coal as fuel. As electrolytes, this technology uses non-porous solid oxide ceramic compounds.

However, these sever operation conditions are a huge obstacle for the longevity of the fuel cell, and very slow start-up.

1.1.1.6 Phosphoric Acid Fuel Cells (PAFCs)

PAFCs uses liquid phosphoric acids as an electrolyte, along with porous carbon electrodes containing platinum for the catalysis process. These technology of fuel cells operate in an intermediate temperature range (150°C-200°C). They use hydrocarbon, such as natural gas, propane or methane as their fuel.

PAFCs are easily poison by carbon monoxide during the catalysis, decreasing its efficiency. These fuel cells are usually very heavy, and since it uses platinum, it makes them very expensive. This technology is usually associated with stationary power generation, although in some cases is used to power city buses.

Table 1.1 Different types of fuel cells and suitable applications

Fuel Cell type	Operating Temperature [°C]	Suitable applications			
		Domestic Power	Small-scale Power	Large-Scale cogeneration	Transport
DMFC	50 - 120	✗	✓	✗	✗
PEMFC	80 - 100	✓	✓	✗	✓
SOFC	800 - 1000	✓	✓	✓	✗
PAFC	200 - 250	✗	✓	✗	N/A
AFC	60 - 90	✓	✓	✗	✓
MCFC	650	✗	✓	✓	✗

1.1.2 Electrolyte

The electrolyte it's often considered as the heart of the fuel cell, since it determines the type of charge carrier transported from the anode to the cathode, it's the medium in which the ionic mobility occurs, and it also determines the operating temperature of the fuel cell.

Currently in the market around 85% of the FC manufactured are design to operate in the low temperature range (below 100°C)[1], and the industry standard for the electrolyte it's a polymer called Nafion, which its limited to run in a low temperature range (~80°C). On the other side of the spectrum, oxides used as electrolytes, are yttrium stabilized zirconia and gadolinium doped ceria that can withstand operational temperatures up to ~1000◦C [9].

However, a huge drawback for low temperature range electrolytes is the need of a humid atmosphere in order to work, also they are permeable to methanol and hydrogen, which lowers fuel efficiency. It's worth mentioning that they don't conduct protons, but rather hydronium ions, which are the cations of water, H_3O.

High temperature range fuel cells on the other hand, have the disadvantage of very high operational temperatures, long start-up times and have mechanical and chemical issues[10].

Addressing these limitations, a lot of efforts have been made to overcome this issues by using electrolytes that can operate at intermediate temperatures. Using electrolytes that works in these temperature range offer several advantages, like an enhanced reaction at the anode, which

allows using other materials than Pt for the catalysis process, resistance to CO poisoning, a more effective water management, and the usage of different fuels other than Hydrogen, like as methanol, ethanol and alcohol [9].

1.2 ALKALI METALS

The metals from the first group of the periodic table are known as alkali metals, they include lithium, sodium, potassium, rubidium, cesium, and francium. This group has interesting properties; their atomic radius increases steady as the atomic numbers increases, but their electronegativity decreases.

1.3 SOLID ACIDS

Solid acids are constituted by cations (any alkali metals) with tetrahedral oxyanions. Usually they are represented by the form $M_aH_b(XO_4)_c$, where M represents alkali metal cations and XO_4 is a tetrahedral oxy-anion. The lower-case letters are integers. Solid acids have a white powder appearance and are soluble in water even at room temperatures and they are proton conductors owing they have protons from the 'acid' structure, but tend to be brittle, just like a salt. When phosphate is used to form the tetrahedral oxyanions, alkali metals lose their outermost electron to form cations with a +1 charge. This allows all of them to form fully hydrogen bonds phosphate solid acids.

The most attractive property of solid acids in its used as electrolytes it's a dramatic 2-3 jump in order of magnitude of proton conductivity when heated. This phenomenon has been label as "Superprotonic conductivity" and is associated with a change of phase [11] and Baranov was the first one to study solid acids as electrolytes[12], [13]. Cesium Dihydrogen Phosphate CsH_2PO_4 (CDP), for example can reach values around 2.2×10^{-2} S cm^{-1} for temperatures above 230°C [14], [15]. The temperature associated with the sudden increase in the protonic conductivity it's labeled as T_{SP}. The highly dynamic disordering of the Hydrogen bond network it's been attributed to the dramatic jump in proton conductivity once T_{SP} has been reached.

Haile *et .al.* were the first group to build an operational proton-exchange membrane fuel cell (PEMFC) using a solid acid, cesium hydrogen sulfate, $CsHSO_4$ as the electrolyte membrane (with a thickness of about 1.5 mm) working in temperatures around 150-175°C in a H_2/O_2 configuration [16]. However, after 18 hours of use at ~ 175°C the electrolyte started to decompose, under normal fuel cell operational conditions, which can be expressed as:

$2CsHSO_4 \rightarrow Cs_2SO_4 + H_2O + SO_3$ with $Cs_2S_2O_7$ appearing as an intermediate byproduct at slow heating rates [17].

In order to overcome the long-term stability issue of $CsHSO_4$, CDP was proposed to be used instead. Haile *et. al.* in 2004 [18] and one year later Otomo *et. al.*[19], successfully constructed a fully operational fuel cell at 240°C, however required a humidified atmosphere [p(H2O) = 0.3 atm] to the electrolyte in order to keep the superprotononic phase stable over time. As address in the abstract, although using a humid atmosphere around the solid acids helps with stabilization of the superprotonic phase, it's a longtime

Unfortunately, at these temperatures the highly conductive phase is not stable, as its starts to dehydrate, unless it's put under a saturated water vapor atmosphere, which delays the dehydration. Another method to stabilize the highly conductive phase is to subject a pressure of 1GPa [20]. However, none of these methods are practical approaches for making full scale and operational fuel cells

As addressed in the abstract, the main purpose of these dissertation is to find an alternative to stabilize the proton conductivity of CDP at intermediate temperatures without the need of a humid atmosphere around the solid acid, or applying a pressure of 1GPa over the electrolyte, since none of these methods are practical approaches for making full scale and operational fuel cells.

Chapter 2: Theoretical Background

2.1 Electrochemical Impedance Spectroscopy

Electrochemical Impedance Spectroscopy (EIS) is a powerful and versatile technique used in a wide variety of analysis, such as concrete corrosion, coatings evaluation, electrodeposition, semiconductors, solid and liquid electrolytes in fuel cells, among others [21], [22].

Since the 1970's EIS have been used for measure ionic mobility in electrolytes. Also, have been used to investigate the mechanisms of electrochemical reactions between the electrode and the electrolyte , and properties of porous electrodes [23].

The EIS used can be described as follows, the sample is placed between two electrodes and an open circuit potential is formed between the electrode/electrode interface, but no net current going through the electrolyte. Then, a potential is applied across the electrolyte and an electrochemical reaction creates an ionic current through it. The sample is typically subjected to a small fixed AC potential (usually between 10mV to 100mV) over a wide range of changing frequencies (6MHz-1Hz) and the ionic current response from the system is measured at each individual frequency.

Since different electrochemical processes are frequency dependent, a range of frequencies can be used as a tool to probe the sample's bulk resistance and to discard the electrochemical processes that have less effect on it such as the electrode polarization, grain boundary conductivity, or the ion transfer.

2.1.1 Basics of Impedance Spectroscopy

On the following section, the basis of impedance will be described to have a better understanding on how EIS works.

2.1.2 Ohm's Law

Ohm's Law establishes the ratio between voltage and current as resistance (Equation 2.1)

$$R = \frac{V}{I} \tag{2.1}$$

Were R is the resistance, V it's the voltage, and I is the current. The resistance is considered as an ideal resistor and its value is independent of the frequency. Intrinsically, the resistance is the material's property to resists the current flowing through it.

Since the EIS technique employs an AC voltage, its value can be expressed as frequency dependent as shown in Equation 2.2

$$V = V_0 \sin \omega t, \tag{2.2}$$

Were V is the voltage, V_0 it's the amplitude of V and t is time. The term ω is radial frequency, express as $\omega = 2 \pi f$, and f is the frequency.

Similarly, the current can be described by equation 2.3

$$I = I_0 \sin \omega t + \theta \tag{2.3}$$

Where I is the current, I_0 it's the amplitude of I and θ is the phase shift between the current and voltage as shown below in illustration 1.

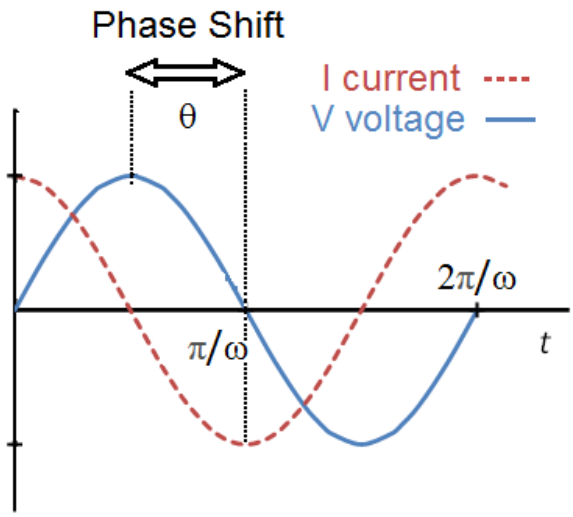

Illustration 2.1: Current, voltage in a ESI system

If we substitute V and I from equations 2.22 and 2.33 into Ohm's Law we get:

$$Z = \frac{V}{I} = \frac{V_0 \sin \omega t}{I_0 \sin \omega t + \theta} = \frac{Z_0 \sin \omega t}{\sin \omega t + \theta} \quad 2.4$$

Equation 2.4 were Z is impedance which is expressed in terms of its magnitude Z_0 and a phase shift.

We replaced resistance by impedance (Z), which is frequency dependent. The impedance, like the resistance, represents the ability to resist the current flowing through the material. However, we can't generalize all the factors that contribute to the resistance as if it only behaves like an ideal resistor; instead we can express all the features that contributes to the resistance as series of electrical circuits elements such as resistors, capacitors or inductors that will represent the equivalent impedance of the system.

Furthermore, by applying Euler's relationship (Equation 5) to the expression given for current and voltage, is possible to express the impedance as a complex function. Now the impedance is in terms of its magnitude and the phase angle θ between the current and voltage.

$$e^{\hat{\jmath}\theta} = \cos \theta + \hat{\jmath} \sin \theta \quad \text{(2.5) Euler relationship}$$

Potential and current after Euler relationship:

$$V_t = V_0 e^{\hat{\jmath}\omega t} \quad (2.6)$$

$$I_t = I_0 e^{\hat{\jmath}\omega t - \theta} \quad (2.7)$$

And substituting these equations 2.6 and 2.77 into equation 2.4, will get equation 2.8 which is a complex equation. Also, can be express in terms of the impedance magnitude and phase shift.

$$Z(\omega) = \frac{V_t}{I_t} = \frac{V_0 e^{\hat{\jmath}\omega t}}{I_0 e^{\hat{\jmath}\omega t - \theta}} = Z_0(\cos \theta + \hat{\jmath} \sin \theta) \quad (2.8)$$

2.1.3 Electrical Circuit Elements

The equivalent impedance of a system can be conveniently compared to a passive electrical circuit network, which is calculated and later compared to the actual EIS response. The most commonly used passive electrical circuit elements [24] to evaluate ESI data are presented as follows.

Circuit Element	Impedance Equation
	$Z_R = R + 0\hat{j}$ Resistor
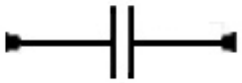	$Z_C = 0 - \frac{\hat{j}}{\omega C}$ Capacitor
	$Z_L = 0 + \omega L\hat{j}$ Inductor
	$Z_W = \frac{1}{Y_0\sqrt{\omega\hat{j}}}$ Warburg Impedance
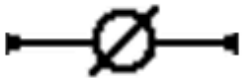	$Z_Q = \frac{1}{Y_0\,(\omega\hat{j})^n}$ Constant Phase

Illustration 2.2 Circuit Elements and its Impedance equivalent equation

2.1.3.1 Resistor

As shown in illustration 2.2 impedance, the resistor has no imaginary part, the phase shift between the current and voltage is zero.

2.1.3.2 Capacitor

The capacitor has no real component and its imaginary component is negative and inversely proportional to the frequency. The current through a capacitor runs 90 degrees out of phase with the voltage.

2.1.3.3 Inductor

The current of the inductor also is 90 degrees out of phase with the voltage, but the impedance is positive and directly proportional to the frequency. Notice how all passive electrical circuits models are frequency dependent.

2.1.3.4 Warburg Impedance

Diffusion of ionic charges at the interface between the electrode and electrolytes is very common in electrochemical processes, this behavior is represented by the Warburg Impedance. Warburg impedance is also directly proportional to the frequency and on the Nyquist Plot appears as a straight line at a 45º since it has identical real and imaginary contributions. It is associated with the resistance to the mass transfer mechanisms. Y_0 is the diffusion admittance.

2.1.3.5 Constant Phase element

One widespread problem when performing the EIS measurements is that the surface of the electrolyte is not homogeneous, thus modelling electrochemical processes cannot use ideal capacitors. Y_0 is the admittance of an ideal capacitance and n is an empirical constant, with values ranging from 0 to 1. When $n = 0$, the impedance behaves like an ideal resistor, on the other hand when $n = 1$ the impedance acts like an ideal capacitor.

2.1.3.6 Electrochemical processes

Several electrochemical processes happen during the EIS measurements. When the initial open circuit potential value of the electrode is changed (by an applying an external potential to the electrodes), an ionic current flow at the electrode surface occurs due to electrochemical reactions; this behavior can be express like an ideal resistor, this effect is known as charge transfer resistance.

Additionally, at the interface between a charged electrode and the ionic electrolyte, ions from the electrolyte are added into the electrode surface, but they are separated by an insulating

space (in the order of angstroms), forming a double layer capacitance. The resistance to the ionic current offered by the electrode is express as an ideal resistor.

2.2 Electrochemical Impedance Spectroscopy Analysis

2.2.1 Equivalent Circuits

To properly model all these electrochemical processes, a network of electrical circuit elements is used to build an equivalent circuit model of the Fuel Cell.

2.2.1.1 Randles Cell.

The mostly commonly used model is the Randles cell circuit and includes the electrode resistance, a double layer capacitor, charge transfer resistance and the Warburg impedance. The charge transfer resistance is connected in series with the Warburg Impedance and they are connected in parallel with the double layer capacitance. This circuit is connected in series with the electrode resistance. This equivalent circuit give a semicircle with a Warburg tail in the low range frequency (Illustration 2.3).

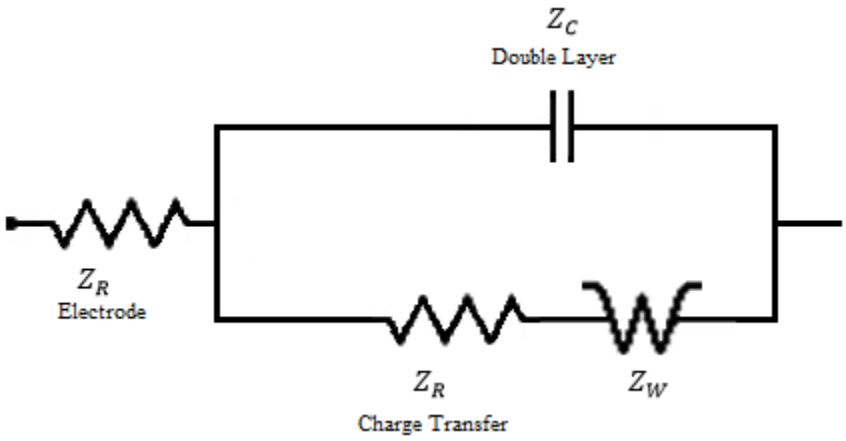

Illustration 2.3 Randles Circuit Model

As described by the Randles circuit model, once the ionic current passes through the electrode resistance (expressed as an ideal resistor), it passes through either the charge transfer

resistor or the double layer capacitor depending of the value of the frequency, the current will take the path of least resistance.

Since the capacitor is inversely proportional to the frequency, at higher frequencies, the capacitor's impedance is decreasing, in which the current tends to go through capacitor rather than through the resistor. On the other hand, at lower frequencies, the capacitor's impedance grows, in which the ionic current passes through the resistor. At this point the entire impedance of the system is expressed as two resistors connected in series. Illustration 2.4 displays this behavior.

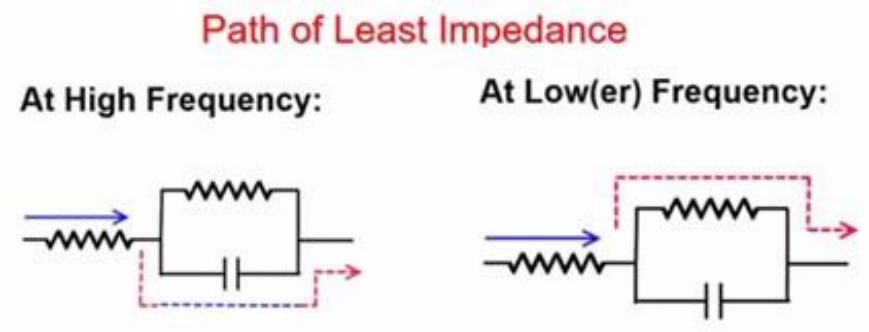

Illustration 2.4 Path of least Impedance

2.2.1.2 Nyquist Plots

A Nyquist plot is formed when the real and negative part of imaginary of the Impedance are plotted forming a semicircle, in which every point of the plot corresponds to a different frequency. The frequencies go from left (high frequencies) to right (low frequencies). The Nyquist Plot for this circuit is shown in Illustration 2.5 [25].

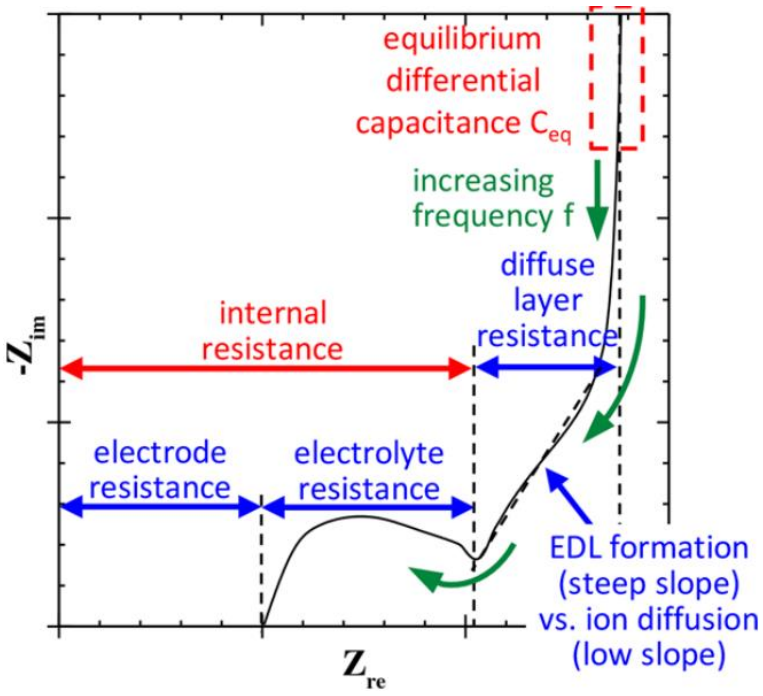

Illustration 2.5 Sections of a Nyquist Plot [25]

2.2.1.3 Electrolyte Conductivity

Illustration 2.6 present the Nyquist plots profiles of the impedance at low conductivity (a) and superprotonic phase (b). Part (a) of the figure shows a semicircle that intercepts the real axis of the impedance at low frequencies, this is considered the electrolyte resistance. On the other hand, part (b) the semicircle is absent, that is because the proton mobility is very large, and in this case the electrolyte resistance is intercept of the straight line with the real axis [26].

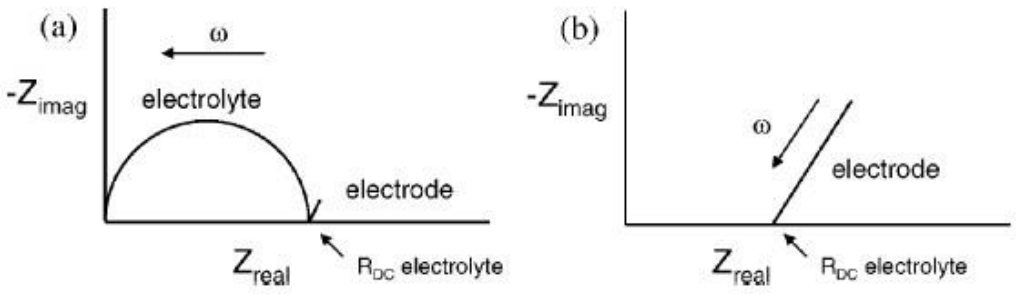

Illustration 2.6 Impedance profiles of low conductivity and superprotonic phases of solid acid compounds [26]

2.2.1.4 Ionic conductivity

Conductivity is defined as the inverse of resistivity and can be express by Equation 2.9

$$\sigma = \frac{1}{\rho} = \frac{l}{RA} \tag{2.9}$$

Where σ is the conductivity, ρ is the resistivity, l is the length of the sample (or thickness), A is the surface area of the sample and R is the resistance of the electrolyte.

Once the electrolyte resistance has been determined by the Nyquist plots, the conductivity of the sample can be calculated from equation 2.9.

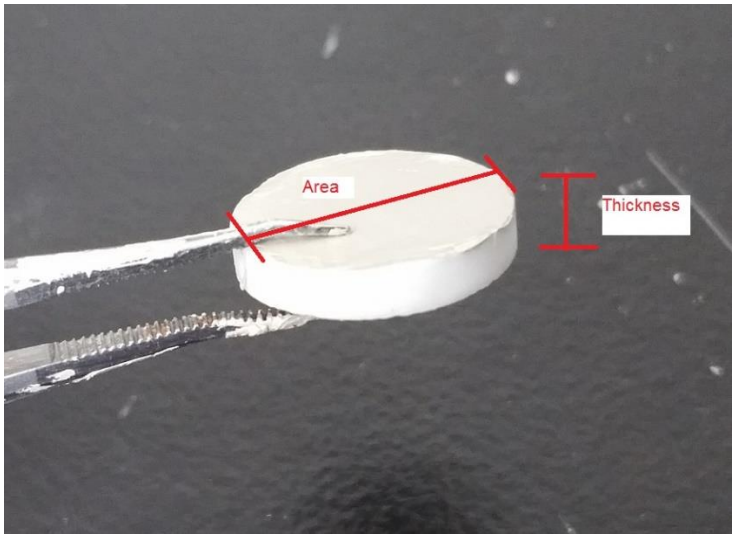

Illustration 2.7 Sample dimensions

2.3 THERMOGRAVIMETRIC ANALYSIS

Thermogravimetric Analysis (TGA) is a characterization technique in which changes in the sample weight are overseen either isothermally or as a function of time as the sample is heated (or cooled) in controlled conditions.

Traditionally a TGA system consists of a sample holder that is supported by a highly accurate precision balance. That sample holder (pan) is inside a furnace and is heated during the experiment. The pan is made from alumina to avoid reactions with the sample.

A sample purge gas controls the sample environment. This gas may be inert or a reactive gas that flows over the sample and exits through an exhaust. Temperature ranges from 25°C to 900°C routinely and not substantial amounts of sample are required, since sample weight range from 1 mg to 150 mg.

TRIOS © software is used to control the conditions of the experiments such as ramp rate, dwell time or gas flow.

2.4 DIFFERENTIAL SCANNING CALORIMETRY

Differential scanning calorimetry (DSC) is a technique used to measure the amount of heat absorbed (endotherm, which are plotted in a downwards directions) or released (exotherm, plotted in an upward direction) by a sample when heated at a constant rate. Using this technique crystalline phase transition and thermal stability of the material can be identified.

2.5 ENERGY-DISPERSIVE SPECTROSCOPY

A very versatile and commonly used characterization technique for elemental composition analysis of a sample is Energy-Dispersive Spectroscopy (EDS). In this technique the sample is bombarded with an electron beam, the interaction of this beam with the solid produces a variety of emissions, X-Rays being one of them. An energy-dispersive detector (EDS) filters the x-rays associated with several elements and creates and energy spectrum. Through the use of software, the energy spectrum is analyzed, and we can determine the

presence of a specific element in our sample. Although in principle this method is able to identify a wide variety of elements, it's more efficient identifying heavier elements with an atomic number Z>11.

Having a flat surface it's preferred to have better results. Finally, accelerating voltages for the electron beam are recommended < 10kV to avoid damaging the sample.

2.6 CRYSTALLINE STRUCTURE

2.6.1 Geometry of crystals

An ideal crystal is defined as infinite repetition of arrangement of atoms (known as unit cells) through space. Unit cells are the smallest unit of a structure used to generate a crystal. This single unit can be arranged in different manners to create the different crystalline structures. An example of a unit cell to generate different crystal structures is shown in illustration 2.8 [27].

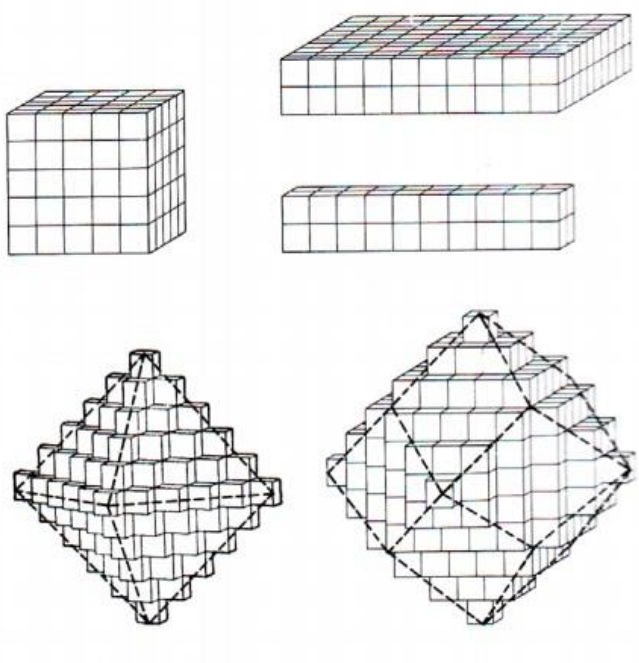

Illustration 2.8 Unit cells forming different crystalline structures [28]

In crystallography, rather than define the crystals in terms of the atoms themselves positioned in a periodic arrangement in 3 dimensions, it's more often to think in terms of a set of imaginary points (known as lattices) which have fixed relation in space to the atoms that form the crystals. They can be seen as the skeleton of the crystal. A point lattice can be viewed as "an array of points in space so arranged that each point has identical surrounding" [29].

Unit cells are known as the basis of the crystalline structure and this basis can be attached to a set of lattices. Arranging the basis at each lattice point will form the entire crystal.

A three-dimensional lattice can be expressed as:

$$r' = r + u_1\overrightarrow{a_1} + u_2\overrightarrow{a_2} + u_3\overrightarrow{a_3} \quad (2.10)$$

The basis must look identical in the point r, as when is translated into the point r' by the vectors $\overrightarrow{a_1}$, $\overrightarrow{a_2}$, $\overrightarrow{a_3}$, where u1, u2, u3 are arbitrary integers. The set of points r' established by Equation 2.10 for all u1, u2, u3 are what defines the crystal lattice.

2.6.2 Crystal symmetries

An important property of a crystal is its symmetry. When certain operations are applied to a crystal, such as rotation (through a certain angle) or translation, and the crystal remains unchanged, then the crystal has a specific symmetry. To fully classify a crystalline structure, all the symmetries must be identified.

Rotation axis: The lattice is rotated in an axis by an angle of $2\pi/n$ radians and remains in its original position. Where n can take the following values n = 1, 2, 3, 4 and 6 and higher and n=5 is no defined. This symmetry it's shown in Illustration 2.9.

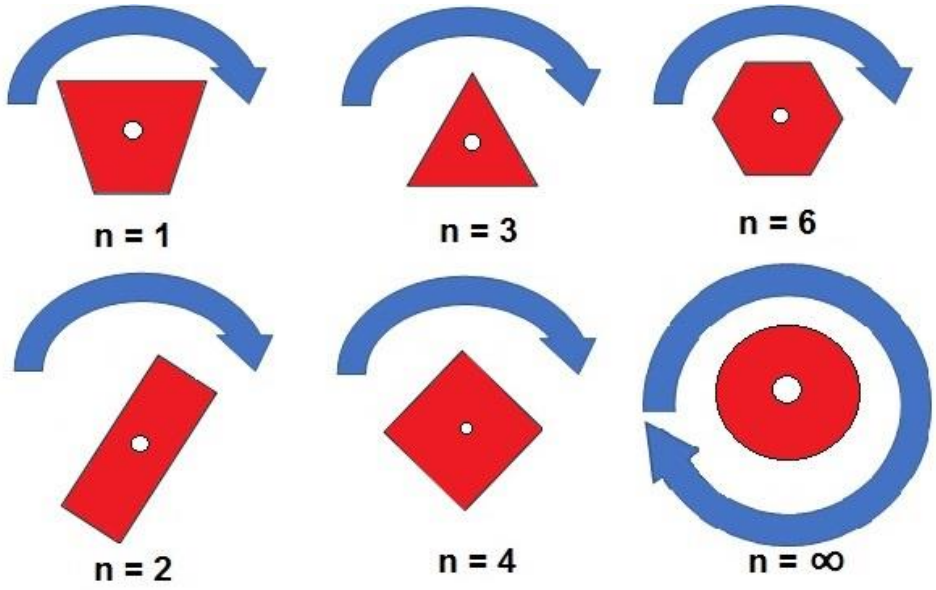

Illustration 2.9 Rotation axis symmetry

Plane of symmetry: Half of the crystal is reflected in a plane, in a way that the reflection passes through a lattice point reproducing the remaining half. The 2D reflection of the crystal occurs across a plane (m). An example is shown in illustration 2.10.

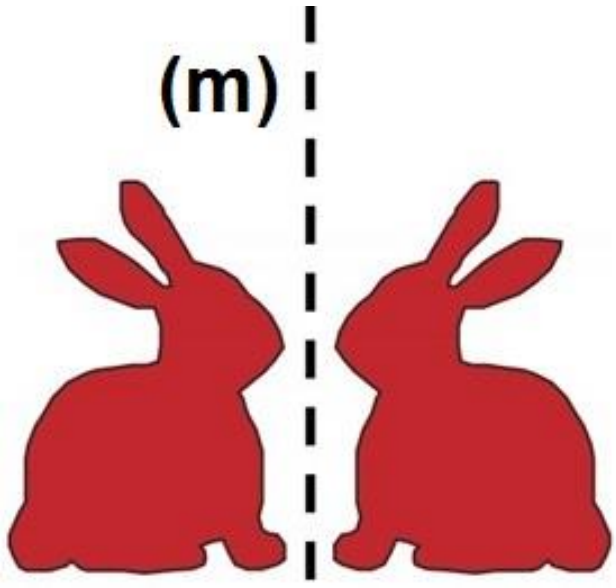

Illustration 2.10 Plane of symmetry

Center of symmetry (inversion): A lattice point in which the distance to r' and the distance to its inverse are –r' are at the same, when this point is placed at the origin, it is said to be the center of symmetry$\bar{1}$.

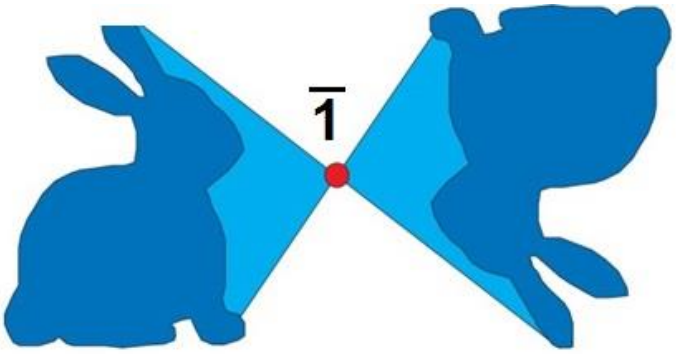

Illustration 2.11 Inversion with a center of symmetry

Translation: When an operation (t) is applied to a point and generates a pattern of identical intervals. Such symmetry is displayed in illustration 2.12.

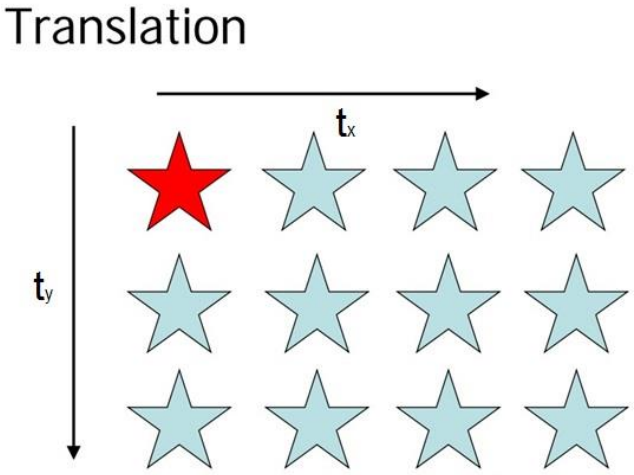

Illustration 2.12 Translation symmetry

2.6.3 Crystal systems

Crystal systems can be categorized according to their lattices and each one possesses three axes in a specific geometrical arrangement and should be stacked to fill three-dimensional space. There are 7 crystal systems with different shapes and forms depending on their lattice lengths a, b and c and their angles between them α, β and γ: Cubic, hexagonal, tetragonal, trigonal (or rhombohedral), orthorhombic, monoclinic and triclinic. The crystal systems are shown in figure 13.

2.6.4 The Bravais Lattices

In 1848 the French Crystallographer Auguste Bravais demonstrated that there are only 14 different ways in which lattice points can be arranged to build the crystal structures.

These different structures can be divided in the different crystal systems and sub divisions: a primitive (P) cells contains only one lattice point per cell, while non-primitive cells have more than one. F means that have a face-centered lattice point, P have a body-centered lattice point, whereas C refers to a base centered cell. The Bravais lattices can be found in illustration 2.13.

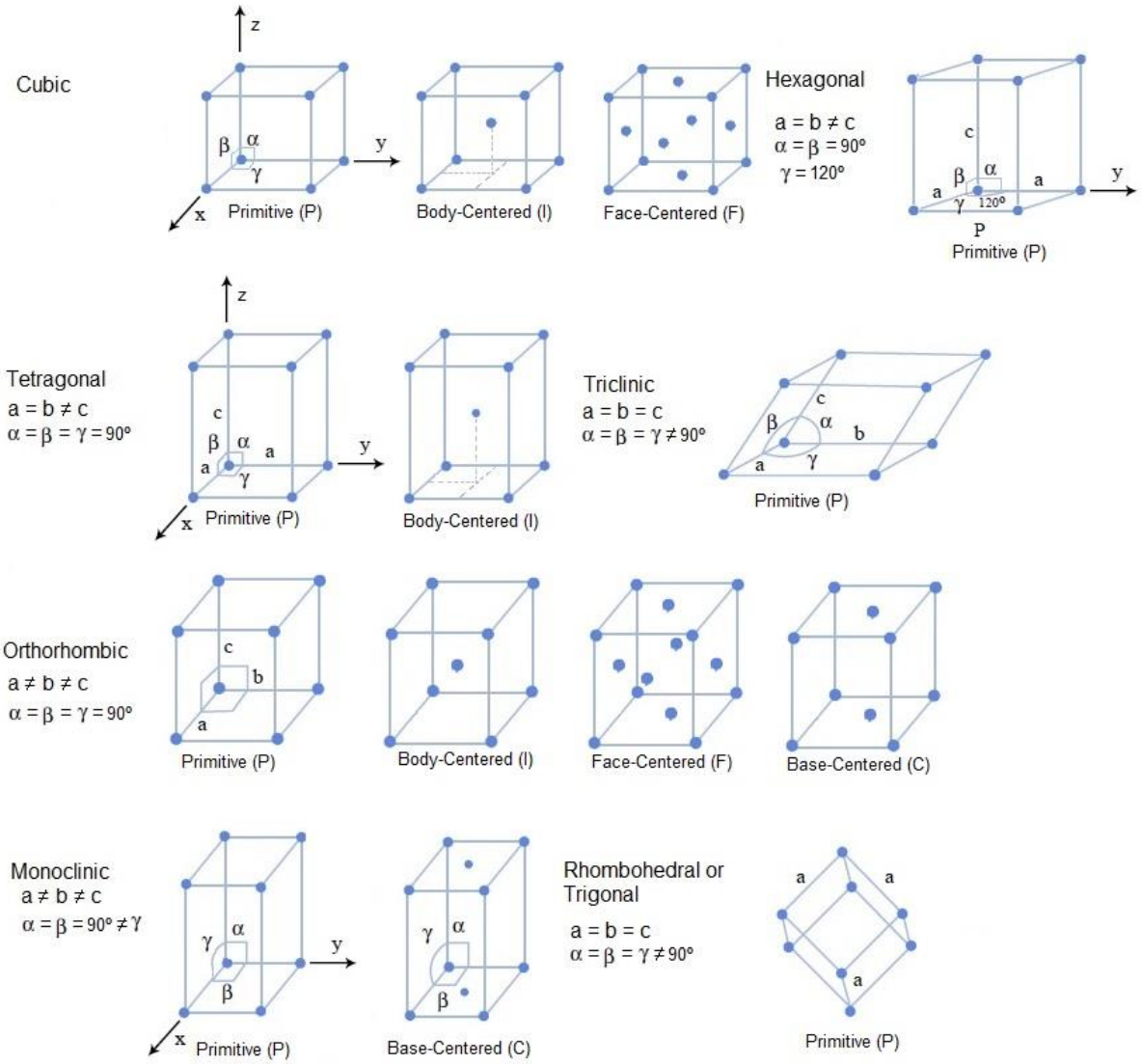

Illustration 2.13 Crystal systems and Bravais Lattices

2.6.5 Space Groups

When a set of non-translational symmetry operations are applied to a crystal group and it remains unchanged, its say to have a space group. The non-translational symmetry operations were discussed previously in the crystal symmetries section.

There are 230 separate ways in which the crystal symmetries can be applied into a crystal group while remaining unchanged. Each one of these possible combinations constitutes a space group.

A crystal can be assigned to one of these groups after the arrangement of its atoms is studied, as by X-ray crystallography, thereby providing a definitive way of categorizing the inherent symmetry of the crystal.

2.6.6 Lattice Planes and Miller indices

A plane, or family of parallel planes, that intercepts periodically with the previously discussed Bravais lattices are known as lattices planes and are described by Miller indices with the values *hkl*. Miller indices are determined as follows [30]:

1. - Locate the points in which the plane intercepts with the a, b, c axes, without passing through the origin. If it does, then the origin must be relocated.

2. - Then take the reciprocals of the interceptions, because in case the plane never intercepts any axis, since then the plane would never intercept at infinity.

3. - For the next step, the reciprocals should be express as rational fractions

4. - Finally, the resulting numbers are put inside parenthesis. Any negative number are written with a bar over it.

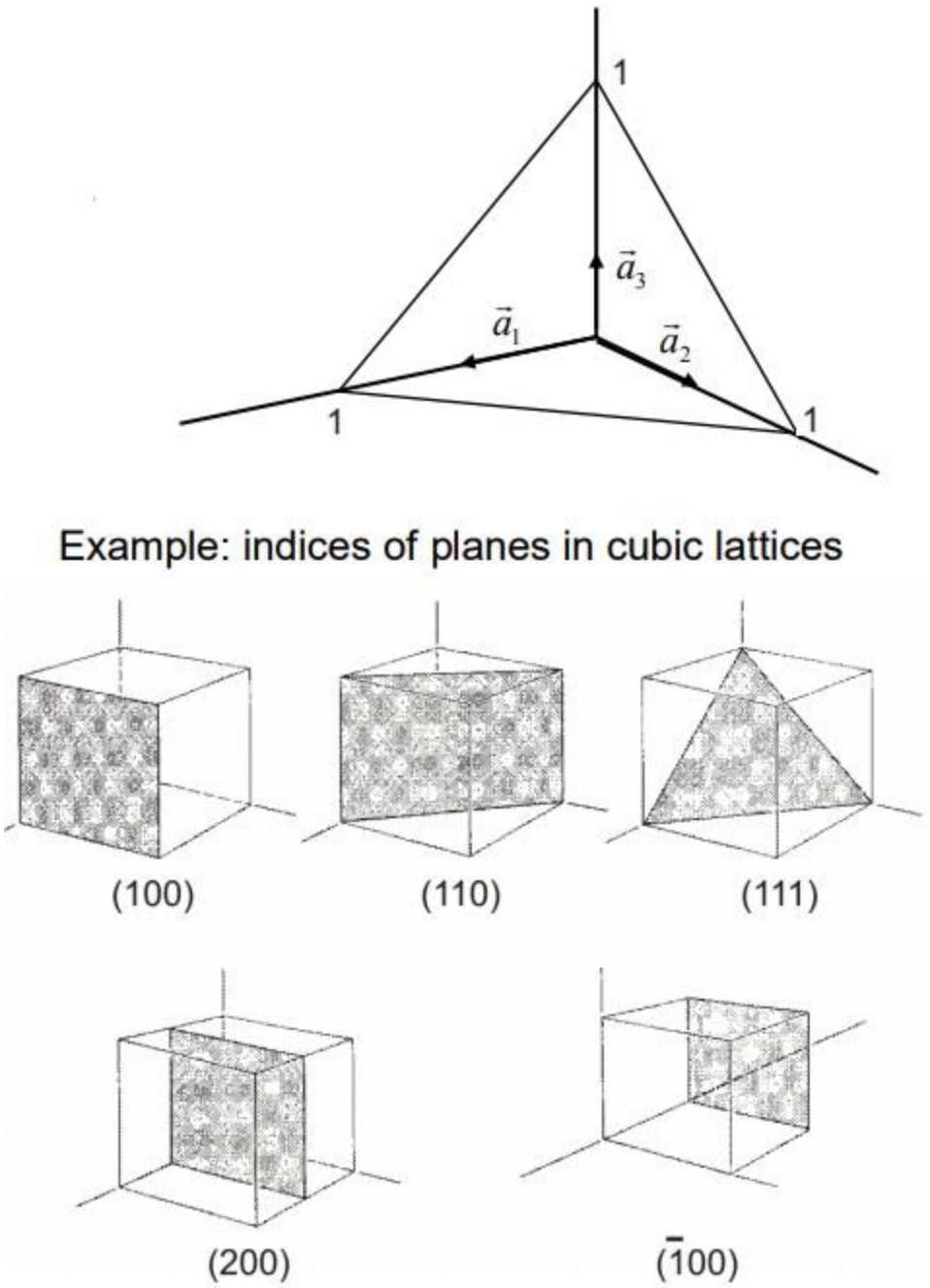

Illustration 2.14. Example of Lattice plane and Miller indices [30]

2.7 X-RAY DIFFRACTION

Getting information of the geometrical structure of matter at atomic level it's a valuable tool to have better understanding of the material's properties. One important analytical technique is X-Ray diffraction, in which, by applying Bragg's law (which will be covered in chapter 2.8.1),

using a fixed wavelength λ and scanning through different angular values of θ, we can obtain the inter plane spacing *d* in a crystalline structure. Through this powerful technique, we can characterize phases and acquire atomic structure parameters. Although Single Crystal X-Ray Diffraction nowadays it's the standard in terms of structural transformation, for this dissertation, X-Ray powder diffraction was utilized, mainly because single crystals began unstable as they crack at elevated temperatures, so powder is the way to go. Also, in our intent to unveil the polymorphic transition of CsH_2PO_4 at different temperatures, using Single Crystal X-Ray Diffraction provides a shift in the polymorphic transition of the solid acid. As reported by Baranov [31], [32], since the dehydration of CDP is slower compared to powder materials.

Besides, this Powder X-Ray Diffraction method offers numerous advantages like its non-destructive nature, high sensitivity, relatively easy sample preparation, fast speed data acquisition (depending on the parameters), high resolution, and through the usage of software, the data interpretation tends to be very user friendly. As long as the sample possess a crystalline structure, this powerful technique has a wide range of applications [33].

2.7.1 Bragg's Law

Bragg's law it's the core behind the X-Ray Spectroscopy technique. The basic idea it's that when incident X-Ray beams (of a specific wavelength) hits the surface of a crystalline material at certain angles, intense peaks of radiation gets reflected from the material. William Lawrence Bragg and its son where the first one to explain this behavior (for which they were awarded the Physics Nobel Prize in 1915), as the X-Rays beam passes through the material, they will get diffracted at different angles depending on the orientation of the plane that of the crystal, but a small fraction of the X-Rays will get diffracted at the same incident angle θ. The intense peaks of radiation mentioned earlier correspond to the constructive interference of the X-Rays from the parallel planes of atoms given by the following equation 2.11 (Bragg's Law):

$$n \lambda = 2 d \sin \theta \tag{2.11}$$

Where n is integer number, λ is the wavelength of the X-Rays, θ is the angle between the incident ray and the crystal planes; and *d* is the distance between the parallel planes of the crystal. Illustration 2.15 shows the schematics of Bragg's Law fulfilled (when the emerging X-Ray it's in phase with the incident Ray and when they are not)

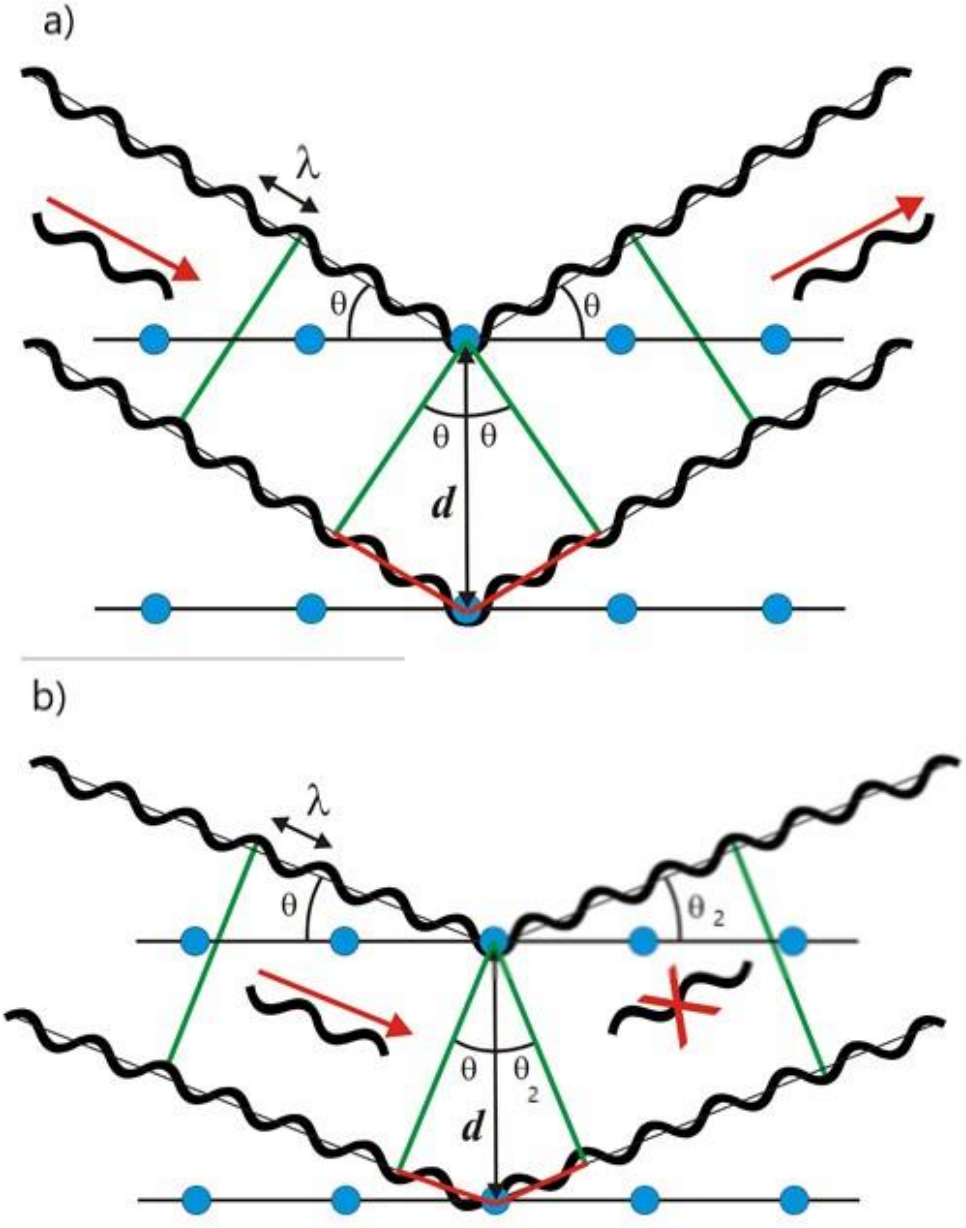

Illustration 2.15 (a) The Incident rays are in phase with the emerging rays fulfilling Bragg's Law (b) Incident rays are not in phase with the emerging X-Rays (if any they are not absorbed by the material) not fulfilling Bragg's Law [34].

2.7.2 Debye-Scherrer cones and data interpretation

In X-Ray Powder Diffraction the sample can be considered as a collection of so many randomly oriented crystallites (about 10^{10} grains in about 1 micrometer of sample), so when incident X-Rays hits the crystallites, the direction of the diffracted rays can have up to 10^{10} different directions (if there is a predominant orientation, will have a defect known as a preferred orientation, this is highly undesirable since it will create systematic error in the observed diffraction peak intensities); giving as a result, whenever the Bragg's Law is fulfilled, a formation of the denominated Debye-Scherrer cones around the direction of the incident beam as shown in illustration 2.16. There are several types of software that allows the integration of these cones and converts them into powder diffraction patterns, where the vertical axis represents the intensity of the reflections and the horizontal axis is given by the 2θ (a typical pattern is shown in figure 2.1). The primary focus of the powder diffraction patterns is determining the material's phase, although determining lattice parameters, crystallites size and even atom positions it's possible. Indexing is defining the set of Miller indices to each Bragg reflections, and fitting the entire profile with arbitrary mathematical functions by the usage of software such as use HighScore Plus or Fullprof, that are not related the atoms, and that provides a very precise determination of the lattice constant. Through the usage of profile fitting we can obtain diffraction peak position, intensity, and width for calculating lattice parameters and crystallite size.

Finally, with the space group determine and the correct lattice parameters, the Rietveld method is used to obtain a more accurate and detailed representation of the unit cell. This model allows a phase identification, and crystallite size calculations, and even it's capable of determining atom positions.

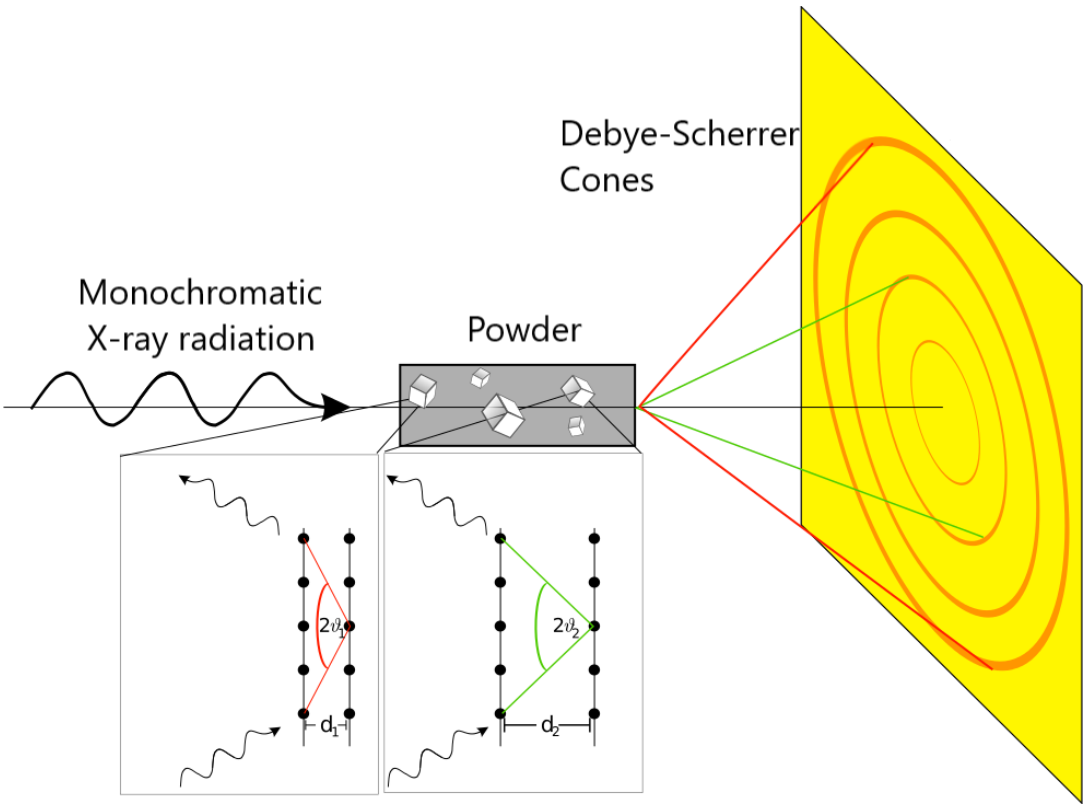

Illustration 2.16 Debye-Scherrer Cones [35].

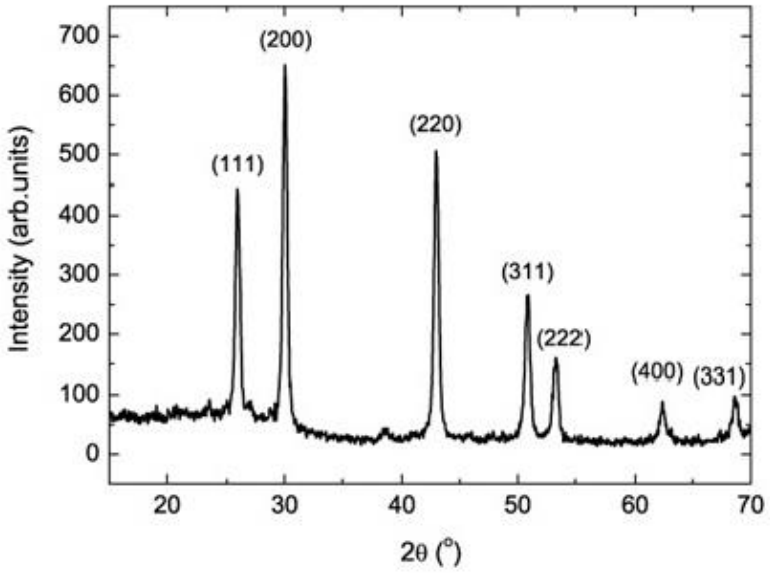

Figure 2.1 Typical XRD pattern of a crystalline structure [36].

Chapter 3: Experimental Details

3.1. Synthesis of (1-x)CsH_2PO_4 / xSiO_2 (0≤x≤0.3) samples

Crystals of CsH_2PO_4 (CDP) were grown by slow evaporation under ambient conditions from an aqueous solution of Cs_2CO_3 (Acros Organics, 99.9%) and H_3PO_4 (Alfa Aesar, 85% w/w aqueous solution) in a 1:2 mole ratio; crystals were then mechanically ground into a fine powder with a mortar and pestle. (1-x)CsH_2PO_4 / xSiO_2 (0≤x≤0.3) composites were synthesized by mechanically dry mixing CDP with silica nano-powder (Sigma Aldrich, 99.8%, 12nm average particle size, specific surface area ~200m^2/g, pH ~ 4, and water content <1.5%).The following mol ratio was employed to fabricate the pellets. Pellets were then pressed at 0.6GPa for 60 seconds using 1g of homogenized powder. Once the pellets were formed, each side of them were painted using silver paint to achieve electrical contacts.

3.2. Characterization procedures

X-ray diffraction (XRD) data recollection was by using a PANalytical Empyrean system with a Cu-*Ka* radiation (λ=1.5418Å) source, illustration 3.1 shows the PANalytical Empyrean system. The system was equipped with an Anton Paar XRK 900 high temperature reaction chamber and a PIXcel^{3D} detector to get data at different temperatures, between 25°C-265°C (shown in illustration 3.2), using a rate of 5°C/min.

Thermogravimetric analysis (TGA) and differential scanning calorimetry (DSC) were performed on a TA Instruments SDT Q600 and DSC Q20 (illustration 3.3), respectively using powder samples kept in air and heated up from room temperature to 260°C at a rate of 5°C/min

Illustration 3.1 PANalytical Empyrean System X-Ray Diffractometer

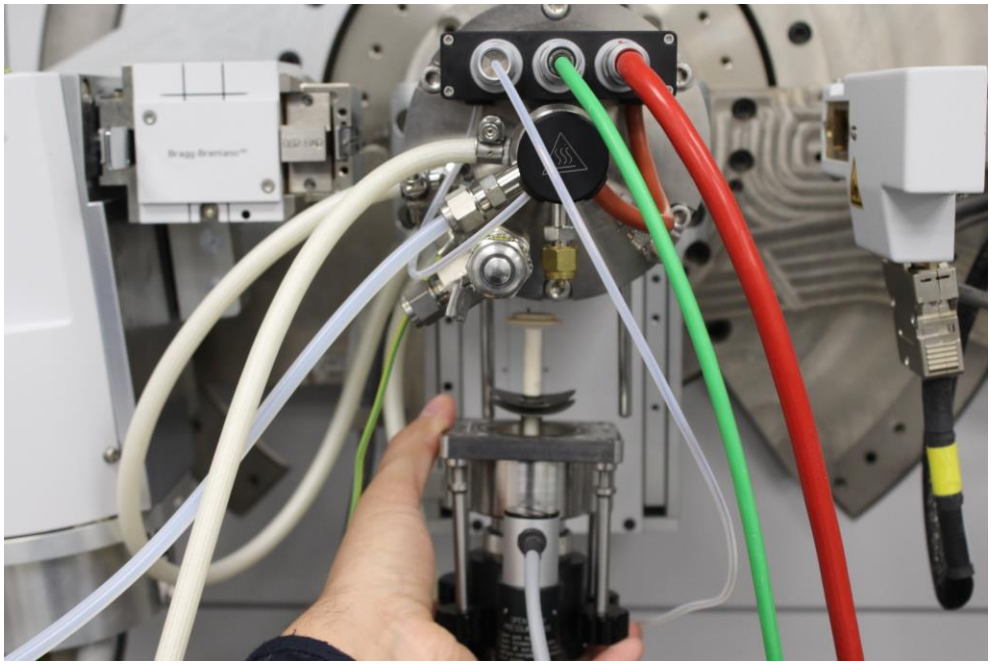

Illustration 3.2 Reaction Chamber XRK 900

Illustration 3.3 TA Instruments SDT Q600 and DSC Q20

An Oxford Instruments attachment with a Hitachi TM-1000 system were used to take Energy-dispersive X-ray spectroscopy (EDS) measurements to confirm the expected $Cs:SiO_2$ ratio for the $(1-x)CsH_2PO_4 / xSiO_2$ ($0 \leq x \leq 0.3$) samples. Illustration 3.4 shows the Oxford Instruments EDS attached with a Hitachi TM-1000.

Illustration 3.4 Oxford Instruments EDS attached with a Hitachi TM-1000

Proton conductivity was obtained using an impedance spectroscopy technique that employs a Solartron 1260 impedance analyzer in tandem with a ProboStat® sample holder. Illustration 3.5 shows the Impedance Analyzer Solartron 1260. This sample holder chamber has a capability of run sample in air and under a humid environment. Illustration 3.6 displays ProboStat® holder. A 100mV oscillating potential in a frequency range from 6 MHz to 1Hz, using a logarithm sweeping, was applied in a standard two-point, four-wire setup. Pt wires were used as measurement leads. The sample holder was placed inside a tube furnace, and the temperature was varied within the 200^0C-260^0C range.

Illustration 3.5 Solartron 1260 impedance analyzer

Illustration 3.6 Probostat® Sample holder chamber

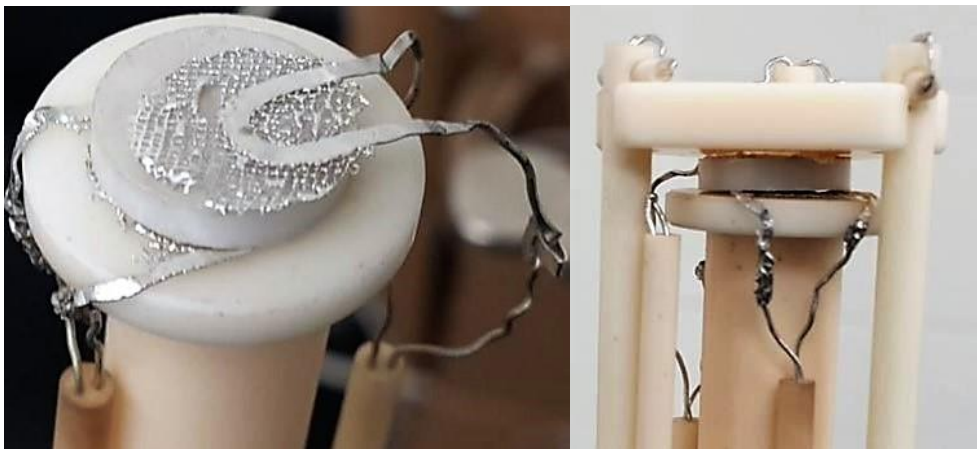

Illustration 3.7 Two-point, four-wire setup using Pt wires set up for impedance measurements

Proton conductivity was determined from Nyquist plots. Measurements were carried out both in dry air (~20% relative humidity (rh)) and in a humid atmosphere. To achieve this condition, the sample was held in a chamber connected to a humidifier that provided an argon gas flow bubbled through a heated water reservoir to reach 0.38atm of H_2O partial pressure at the sample. The humidity was adjusted by controlling the water temperature in the reservoir. Illustration 3.8 shows the Impedance Spectroscopy system used for the experiment

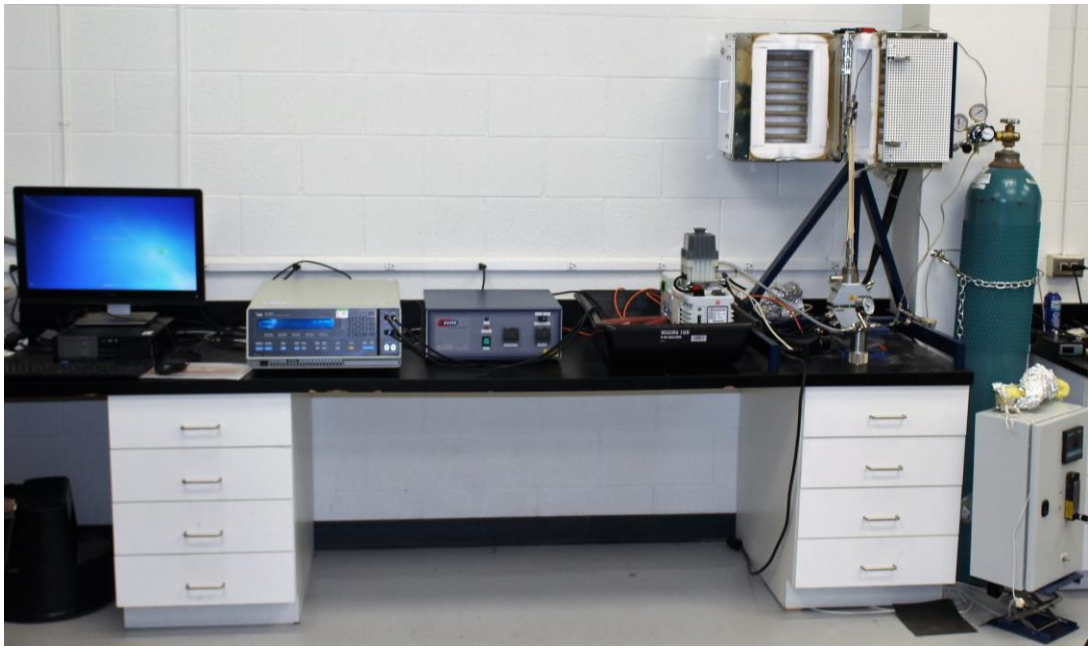

Illustration 3.8 Impedance Spectroscopy system

Chapter 4: Results and Discussion

4.1. X-RAY DIFFRACTION AND THERMAL ANALYSIS OF THE SUPERPROTONIC PHASE

We started our analysis by taking X-Ray Diffraction data of neat CsH_2PO_4 at room temperature in order to corroborate that CsH_2PO_4 have monoclinic phase ($P2_1/m$) at room temperature as previously reported by several researchers (Baronov, Otomo, Boysen and Haile)[12], [18], [37]–[42] . Figure 4.1 shows a Rietveld refinement against x-ray data obtained at room temperature from powder of neat CsH_2PO_4. The solid symbols represent the x-ray intensity measured as a function of two theta (between 10^0- 60^0), the solid line is the best possible Rietveld fit, and the vertical tick bars are the Bragg reflection markers. At the bottom of the figure, the lower trace represents the difference curve between the calculated and the observed XRD patterns: I_{calc}- I_{obs}. To obtain the closest agreement with the data, the Rietveld refinement adjusted the unit cell parameters, peak profiles, atom positions and the Debye-Waller thermal parameters. The initial parameters of lattice parameters and space groups used for the Rietveld refinement came from the PDF # 84-0122. The refinement used converges upon the simultaneous variation of 18 independent parameters to a whole-pattern residual R_{wp}=5.22%. As expected, these results show a monoclinic $P2_1/m$ crystal structure at room temperature that are in agreement with previous studies.

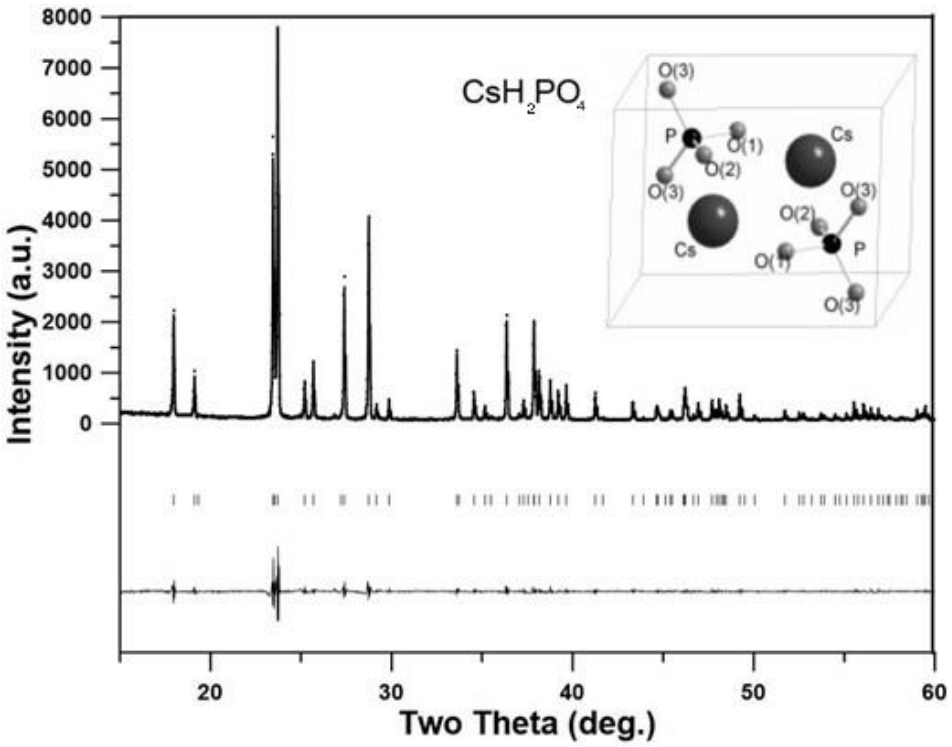

Figure 4.1 XRD Results for CsH2PO4 at room temperature

Following the aforementioned study and to have a better understanding of the polymorphic phase evolution from a monoclinic phase ($P2_1/m$) at room temperature to cubic (Pm-3m) at high temperatures of CsH_2PO_4, a temperature dependence study of the XRD was performed using neat CsH_2PO_4 in powder form heating the sample in air at a rate of ~5^{o}C/min as shown in figure 4.2

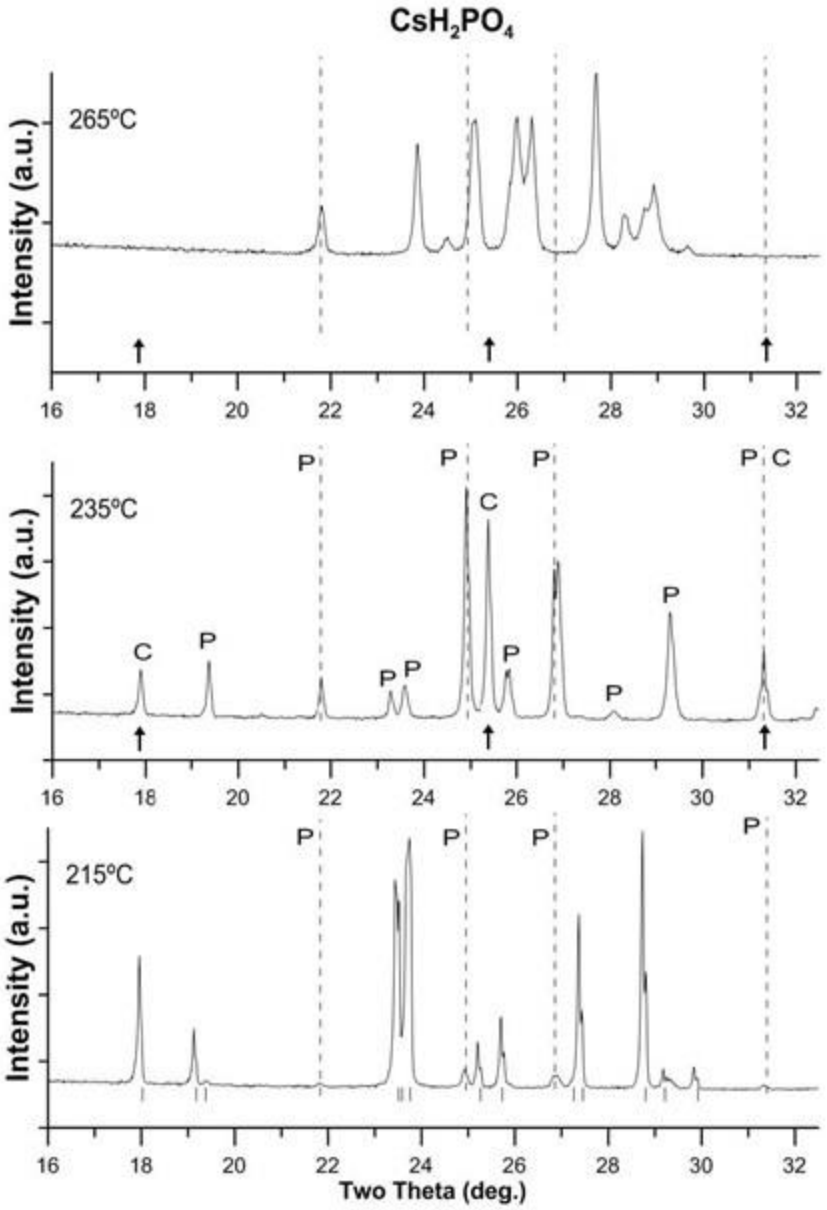

Figure 4.2 Temperature-resolved (215°C to 265°C) XRD results upon heating CsH_2PO_4

The results are presented in figure 4.2. At T=215ºC most of the Bragg reflections (Thickmarks) correspond to the monoclinic phase $P2_1/m$; however, an interesting observation is that there are present weak reflections from Cs pyrophosphate, $Cs_2H_2P_2O_7$ (angular positions of these reflections are marked by vertical dashed lines corresponding to PDF # 45-0619), that's a signal that the material started to dehydrate. Once T reaches T_{SP}, 235ºC, the data exhibits a mixture

of two phases; there are strong reflections from the cubic Pm-3m CDP phase (angular positions corresponding to PDF # 45-0618 marked by vertical arrows). On the other hand, there is presence of the dehydrated product $Cs_2H_2P_2O_7$ (labeled as P). It's worth mentioning that the four $Cs_2H_2P_2O_7$ reflections saw at 215ºC, along the dashed lines, grow stronger.

Finally, well above T_{SP}, at T=265ºC, both the pyrophosphate and the cubic CDP peaks disappeared and the entire XRD pattern corresponds to the final decomposition product(s) of CDP; this pattern is the same as the one reported in [43].

This study provided key information to have a clear picture of the polymorphic phase transition of CDP from monoclinic to cubic. At T= 215ºC there is indication that of dehydration of CDP started since there is the presence of $Cs_2H_2P_2O_7$, that's even before the cubic phase have been appear. This means that it is the monoclinic $P2_1/m$ phase that dehydrates, which differs from previous results on CDP powders [15].

Followed by the XRD analysis and to obtain more information about the phase changes, a thermal analysis on CsH_2PO_4 was performed by heating the sample in air from 100ºC up to 260ºC.

The heat rate was the same of the XRD study, 5Cº/min. The thermal analysis was carried out by thermal measurements using differential scanning calorimetry (DSC), and thermogravimetric (TG). In addition to the measurements on CsH_2PO_4, the same study was performed by adding nano-silica to CsH_2PO_4 to obtain $(1-x)CsH_2PO_4$ / $xSiO_2$ composites, for x=0.2 & 0.3, measured under the same conditions, since these two compounds will be later used in an Impedance Spectroscopy analysis, as they present as an alternative to improve protonic conductivity stability.

Figure 4.3 (a) shows the DSC trace for each compound, CsH_2PO_4 presents a very prominent endotherm at ~232°C which coincides with the polymorphic transition from monoclinic ($P2_1/m$) into cubic (Pm-3m) shown by the XRD temperature resolved analysis on CsH_2PO_4. Therefore, we can attribute this endotherm to the polymorphic transition on CsH_2PO_4. To the right of the aforementioned results, $(1-x)CsH_2PO_4$ / $xSiO_2$ (x=0.2) shows a weak endotherm around 202°C and a more prominent at ~232°C.

(1-x)CsH_2PO_4 / xSiO_2 (x=0.3), also present a big endotherm at ~232°C and a weak endotherm at 210°C. All three compounds exhibited big endotherms around ~232°C, as mentioned earlier, are associated with the polymorphic transition from monoclinic into cubic. However, the two weak endotherms at 202°C and 210°C can be explained as a chemical modification, but further research is required. Figure 4.3 (b) show the (TG) results recorded from the same temperature range 100°C – 260°C. The solid line (TG) shows the overall mass loss in (1-x)CsH_2PO_4 / xSiO_2 composites, about 2.5wt% for x=0, 5.8wt% for x=0.2 and 5wt% for x=0.3 upon heating the samples to 260°C.

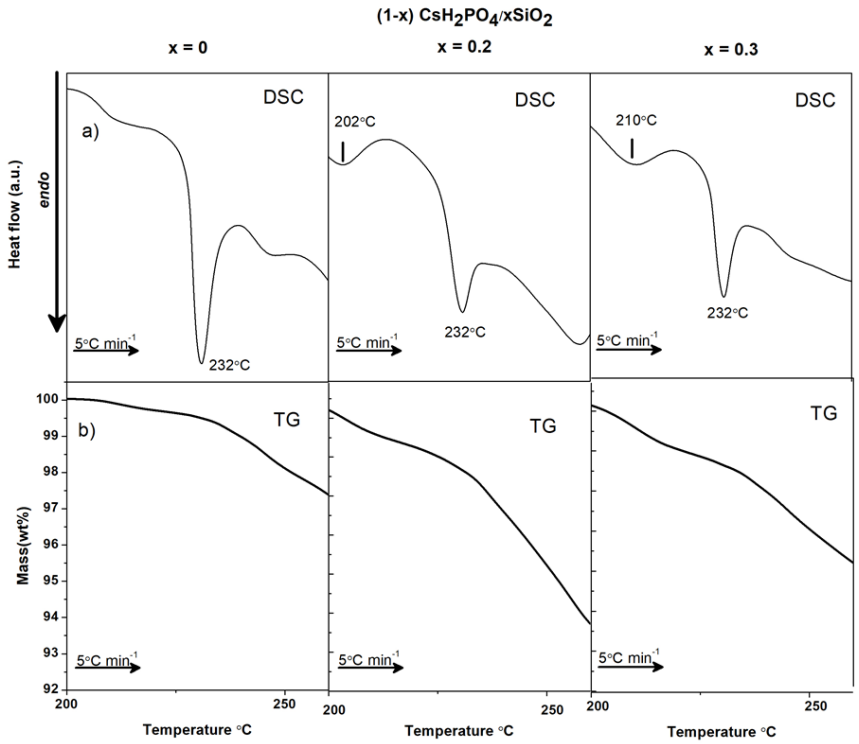

Figure 4.3 Temperature-resolved (200°C to 260°C) DSC and TGA results of CsH_2PO_4

Finally, energy-dispersive x-ray spectroscopy (EDS) was used to corroborate molar composition of the (1-x)CsH_2PO_4 / xSiO_2 composites, for x=0.0, 0.2, and 0.3. EDS results are presented in Table 4.1. The EDS results shows the compositions values are within the margin of error around 4% shorter than the values expected.

Table 4.1 Energy-dispersive x-ray spectroscopy results of (1-x)CsH_2PO_4 / xSiO_2 composites (X=0.2 & 0.3)

(1-x)CsH_2PO_4 / xSiO_2 sample	Expected composition (from synthesis)	Measured composition (form EDS)
x=0.2	80%CDP / 20%SiO_2	76%CDP / 26%SiO_2
x=0.3	70%CDP / 30%SiO_2	66%CDP / 34%SiO_2

4.2. IMPEDANCE SPECTROSCOPY RESULTS ON (1-X)CSH_2PO_4 / XSIO_2 (X=0)

A temperature based impedance spectroscopy study on neat CsH_2PO_4 from 200°C – 260°C over a range of frequencies between 6MHz to 1Hz was executed. The sample was inside a chamber filled with air with a 20%rh and was heated inside a tube furnace at a rate of ~5°C/min.

Figure 4.4 present the Nyquist plots of the sample measured at T=200°C (triangles), T=210°C (circles) and T=220°C (rectangles) upon reducing the measurement frequency from 10^6Hz. In all three temperatures, the semicircles intersect the real axis of the impedance at a frequency of 10^3Hz and, as described in Chapter 2, these intersections with real impedance axis are used to calculate the proton conductivity, σ, in conjunction with the pellet dimensions. It is noticeable that, as the temperature is increased, the diameter of the semicircles decreases. Figure 4.5 focuses on the Nyquist plots on temperatures above T_{SP}: T=240°C (squares), T=250°C (circles) and T=260°C (triangles). These datasets include a broader frequency span – from 10^6Hz to 1Hz – and a clear difference is, that instead of having a semicircle shape (like in lower temperature below T_{SP}), they include a very prominent linear segment and a small semicircle in the high frequency range. This is an indicative of an enhanced proton conductivity. As the Nyquist plots go from semicircle shape (at temperatures below T_{SP}) to straight lines (at temperatures above T_{SP}) is an indicative that the superconductivity phase has been reached.

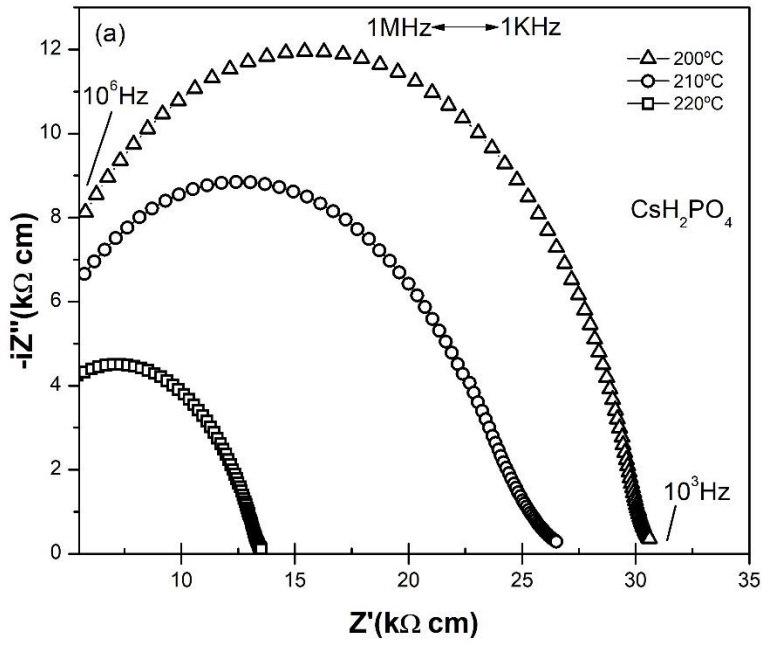

Figure 4.4 Nyquist Plots for CsH_2PO_4 in temperatures below T_{SP}

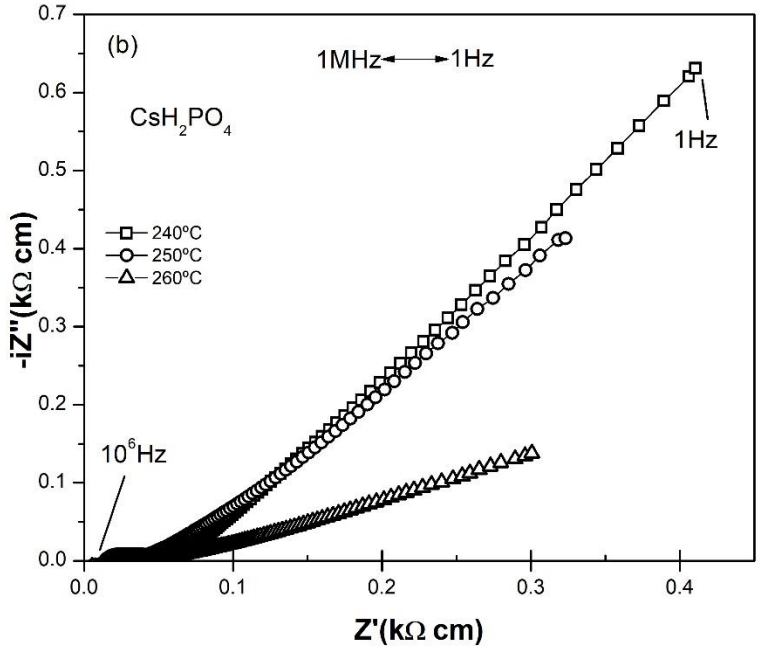

Figure 4.5 Nyquist Plots for CsH_2PO_4 in temperatures above T_{SP}

The proton conductivity was calculated at T=200ºC $\sigma=5.6X10^{-6}Scm^{-1}$ and when it is compared with T=260ºC the proton conductivity value had a three-jump order of magnitude $\sigma=3.6X10^{-3}Scm^{-1}$. The small semicircle at high frequencies has been previously observed [41], [44], [45] and is attributable to the presence of other phases in the sample (in addition to the superprotonic phase).

Figure 4.6, which shows the proton conductivity, σ, calculated for Temperatures between 200ºC to 260ºC. The proton conductivity presents a jump of three-order-of-magnitude between 230ºC-235ºC, which is in accordance with what has been previously stablished. As the XRD study showcased, the dehydration had already initiated at 220ºC, before the proton conductivity jump started, therefore, the sample is a mixture of cubic CsH_2PO_4 and Cs pyrophosphate ($Cs_2H_2P_2O_7$) during the transition to the superprotonic phase.

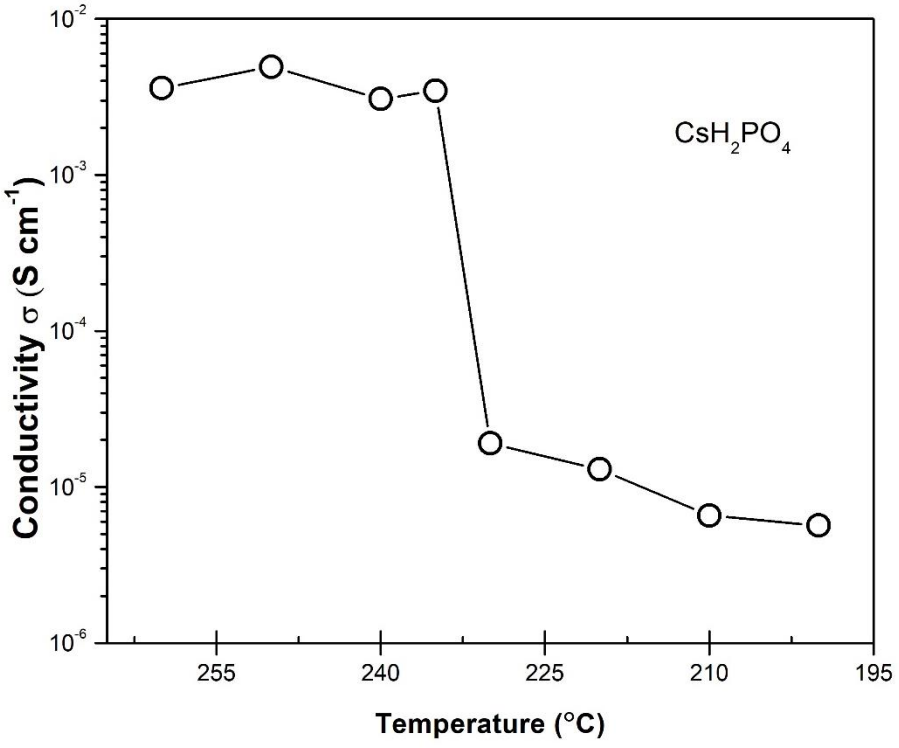

Figure 4.6 Temperature resolved proton conductivity for CsH_2PO_4

At T= 260ºC, the superprotonic phase remains; however, there is no CsH_2PO_4 phase detectable, that means that the sample exhibits superprotonic values past its chemical decomposition. These findings are relevant because for over two decades, there has been a debate in the community about the reason of the superprotonic phase in CsH_2PO_4; some studies attribute this to a chemical decomposition via dehydration[12], [18], [37]–[40], [42], [45] while Ortiz et al. argue a polymorphic transition as the cause [46], [47]. Our results agree that the superprotonic behavior of CsH_2PO_4 is associated with a polymorphic transition rather than a chemical decomposition via dehydration.

4.3. EFFECT OF SiO_2 ON THE SUPERPROTONIC CONDUCTIVITY OF $(1\text{-}x)CsH_2PO_4 / xSiO_2$

To determine the effect of nano-silica on the proton conductivity of CsH_2PO_4, we carried out an impedance spectroscopy study, using the same parameters used for the neat CsH_2PO_4, on $(1\text{-}x)CsH_2PO_4 / xSiO_2$ (x=0.2 & 0.3) samples. Figure 4.7 shows Nyquist plots of x=0.2 by sweeping the frequency from 10^6 Hz to 1 Hz at three temperatures above T_{SP}: T=240ºC (squares), T=250ºC (circles) and T=260ºC (triangles). The data indicate that by adding nano-silica to CsH_2PO_4, the protonic conductivity of the samples is improved. Indeed, the semicircles at high frequencies (observed on pure CsH_2PO_4) vanishes, and significantly higher values of σ are obtained from the intersection of the linear segments with the horizontal axis.

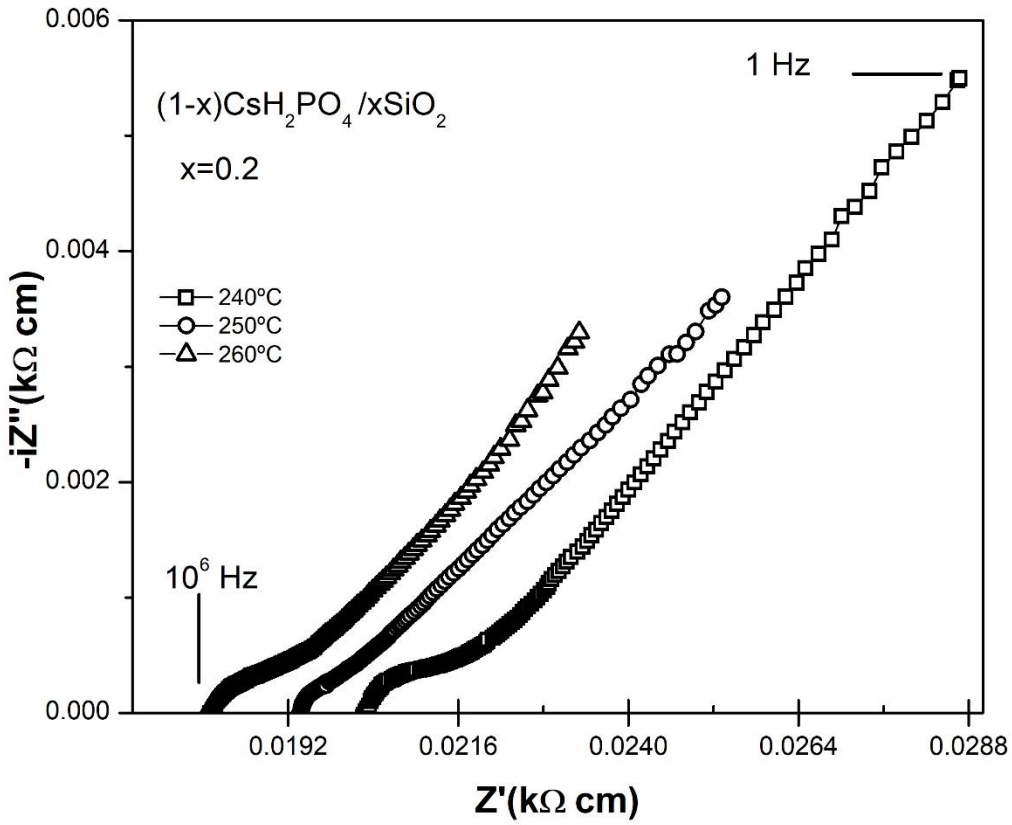

Figure 4.7 Nyquist Plots for (1-x)CsH2/xPO4 for x=0.2 in temperatures above TSP

Figure 4.8 shows the Nyquist Plot for x=0.3 compound at 240ºC (squares), 250ºC (circles) and 260ºC. As in the previous cases at 240ºC and 250ºC there are no semicircles at low frequencies with prominent linear segments, showing a superprotonic behavior and having a proton conductivity of $\sigma=4.8X10^{-3}Scm^{-1}$at 240ºC and $\sigma=5.6X10^{-3}Scm^{-1}$ at 250ºC accordingly. However, a very drastic change happens at 260ºC, where a small semicircle intersects the real axis of the impedance at 120Ωcm showing $\sigma=1.6X10^{-3}Scm^{-1}$ which marks a decay of the superprotonic phase.

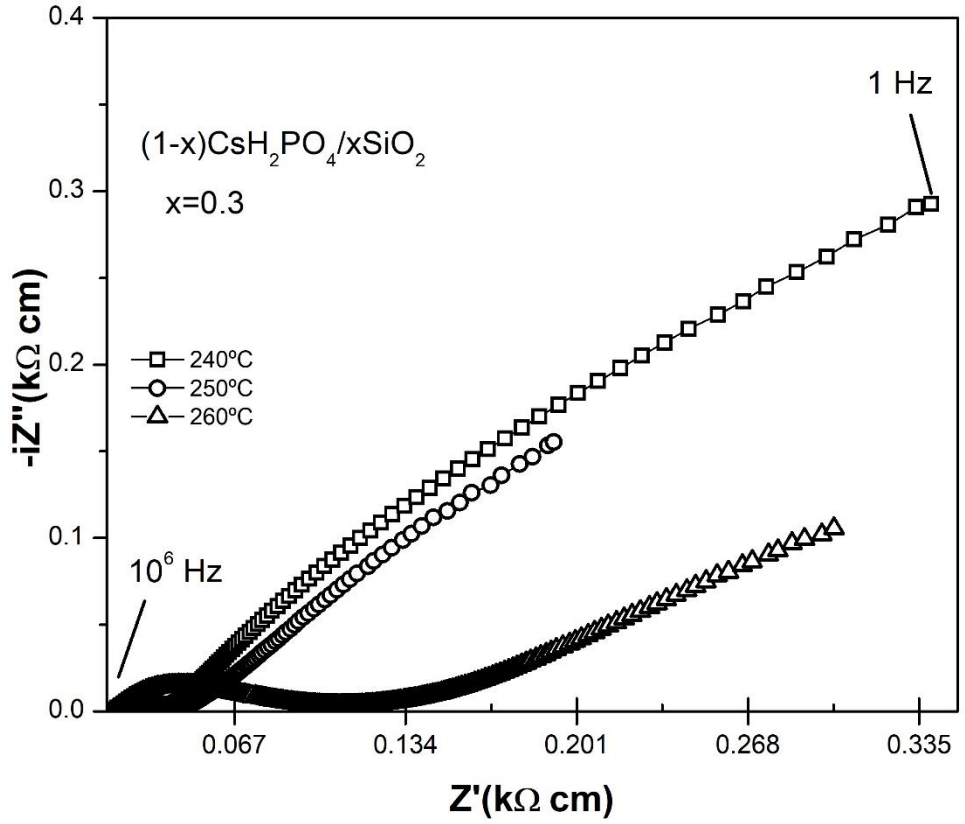

Figure 4.8 Nyquist Plots for (1-x)CsH2/xPO4 for x=0.3 in temperatures above TSP

The proton conductivity for (1-x)CsH2/xPO4 ($0 \leq x \leq 0.3$) is displayed in figure 4.9. At temperatures below T_{SP} x=0.2 & 0.3 exhibit higher conductivity than neat CsH_2PO_4 (x=0); however, neat CsH_2PO_4 have a bigger increase in its proton conductivity at $T_{SP,}$ with three-order of magnitude jump in σ, when the x=0.2 increased two orders of magnitude and x=0.3 had only one order of magnitude increase in its proton conductivity. Also, x=0.3 starts to decrease its proton conductivity after 240ºC.

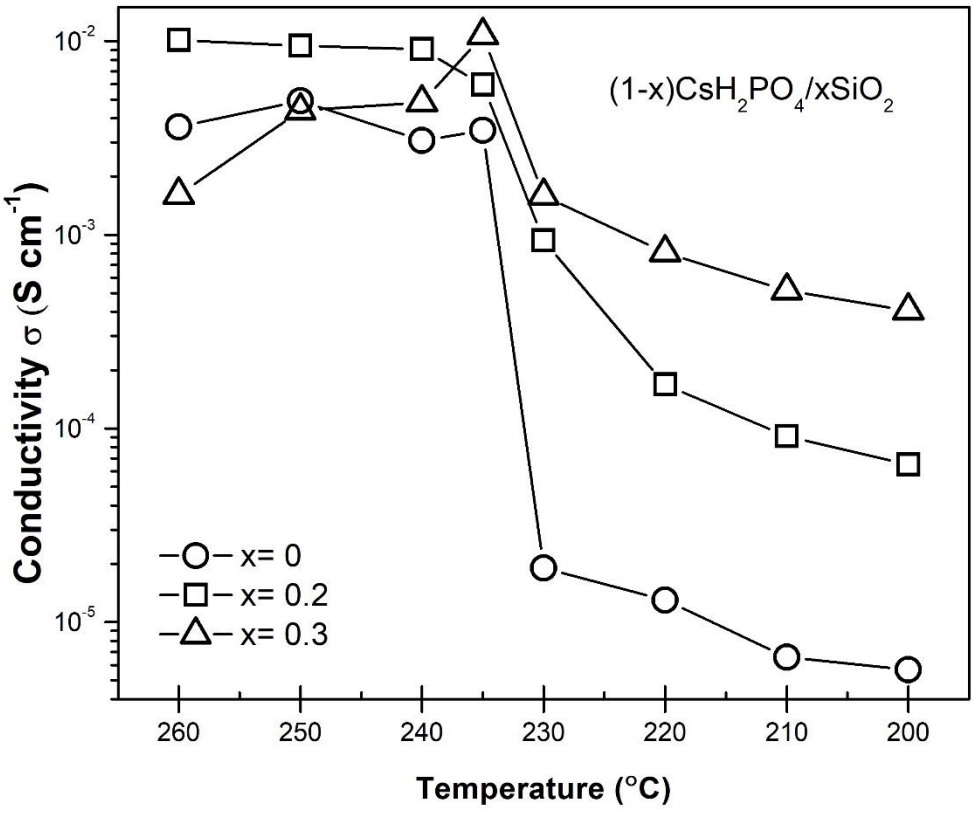

Figure 4.9 Temperature resolved proton conductivity for (1-x)CsH_2PO_4/xSiO2 ($0 \leq x \leq 0.3$)

4.4. STABILITY OF SUPERPROTONIC CONDUCTIVITY OF CsH_2PO_4 IN AIR AND HUMID CONDITIONS

Following the previous analysis, we carried out a 10 hours isotherm study (at 260ºC) of the proton conductivity of CsH_2PO_4 in air (with a~20%rh) and under high humidity conditions (0.38atm of H_2O partial pressure).

Figure 4.10 (a) uncovers the proton conductivity *vs.* time dependence measured on neat CDP under air (squares) and high humidity, under a partial pressure P_{H_2O}=0.38atm (circles). As expected, the superprotonic conductivity is highly stable under humid conditions, i.e. $\sigma \sim 10^{-2} S \cdot cm^{-1}$ changes very little over a 10h timespan, since it have been reported in the past. In contrast, the time-resolved results in air reveals a steady and rapid decrease of the proton conductivity by more than two orders of magnitude after 10h. This behavior agrees with previous observations (e.g. in [45]), except for the high conductivity value in air at t=0. A similar study was performed on the

x=0.2 compound and the results are shown in Figure 4.9 (b). The proton conductivity of the compound under humid conditions exhibits a slight decrease from $10^{-2}S\cdot cm^{-1}$ to $4\times10^{-3}S\cdot cm^{-1}$ over a 10 hours timespan. As seen in figure 4.9 (b), a key observation is that regardless of the environment of the x=0.2 compound, the sample is not as stable over time as CsH_2PO_4 under a water vapor partial pressure.

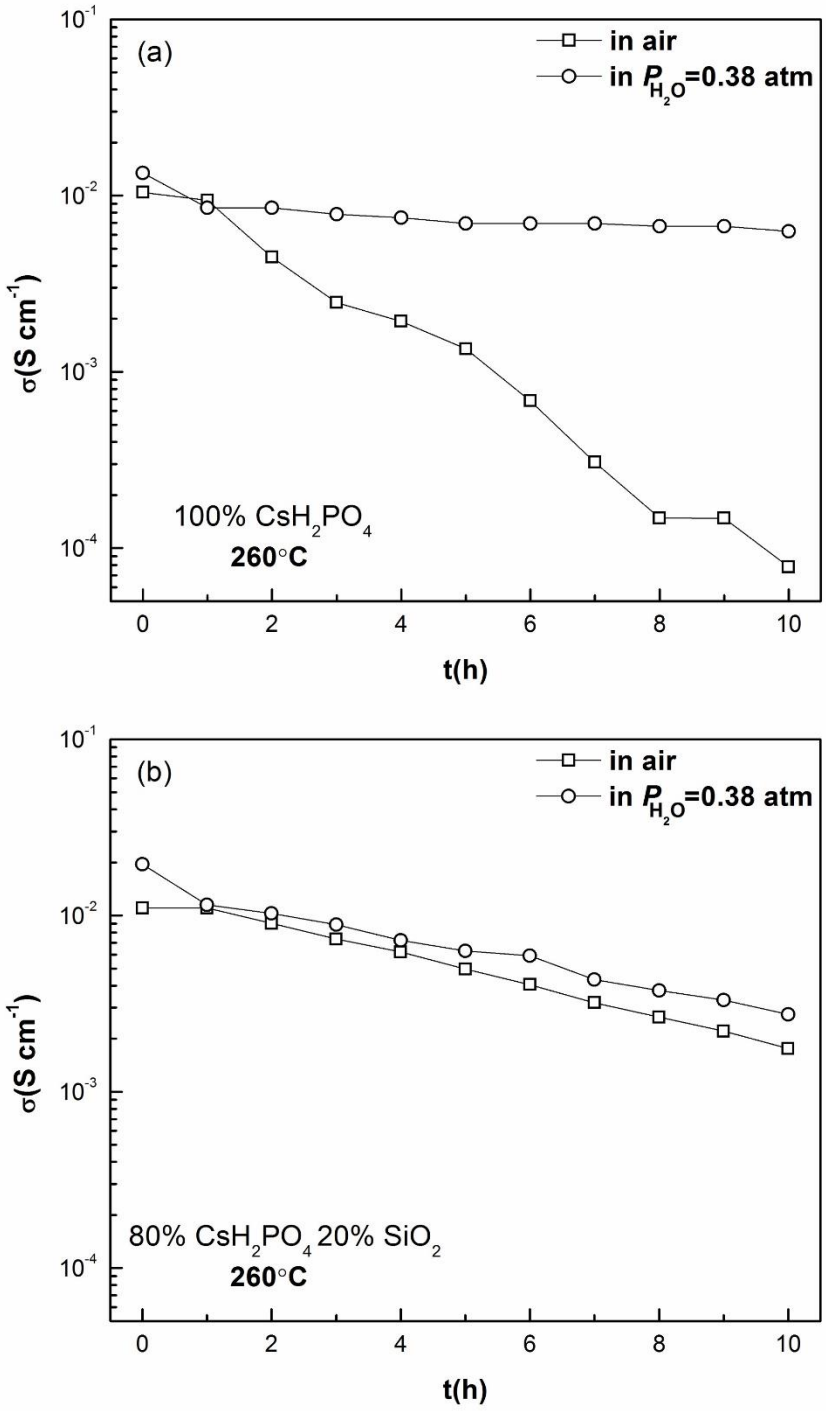

Figure 4.10 Isotherms (260ºC) proton conductivity time study for (1-x)CsH_2PO_4/xSiO_2 (x=0 & 0.2) under both conditions in air (~20%rh) and high humidity (PH2O=0.38atm)

4.5. EFFECT ON THE SUPERPROTONIC CONDUCTIVITY OF CsH_2PO_4 USING HERMETICALLY SEALED CHAMBERS AND UNDER VACUUM

The next step of the research involves study the effect on the superprotonic phase of CsH_2PO_4 by putting the sample inside hermetical sealed chambers of different volumes and under vacuum. The impedance spectroscopy study was executed with the same parameters as the previous studies. The hermetically sealed chambers had the following volumes: 20ml, 47.5ml and 160ml, and chamber with the capability to pull out vacuum had a volume of 50ml. Illustration 4.1 and 4.2 show the different chambers used for the experiment.

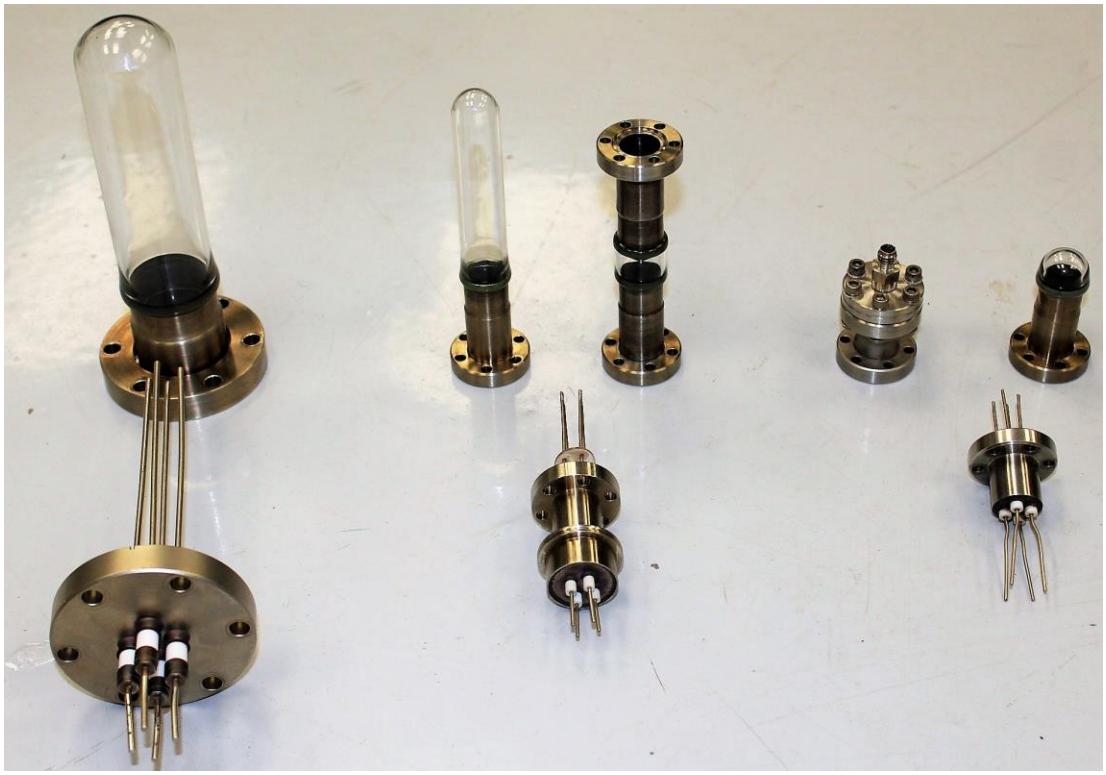

Illustration 4.1 Hermetically sealed chamber (from left to right):160ml, 50ml, 50ml (vacuum), 20ml with the capability of fill gases, 20ml.

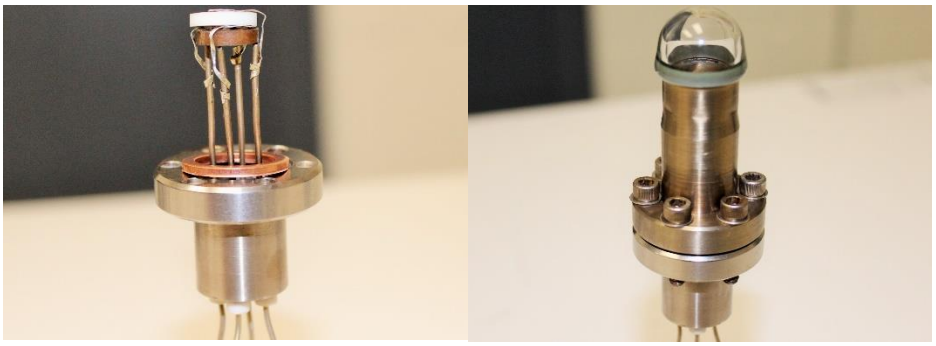

Illustration 4.2 Hermetically Sealed 20ml Chamber. Set up (Left) Ready to use (Right)

Figure 4.11 show the Nyquist plots of the samples measured at T=240ºC (circles), T=250ºC (squares) and T=260ºC (triangles) for each chamber. In all cases, the samples reach surperprotonic phase showing small semicircles at high frequencies along with a predominant linear.

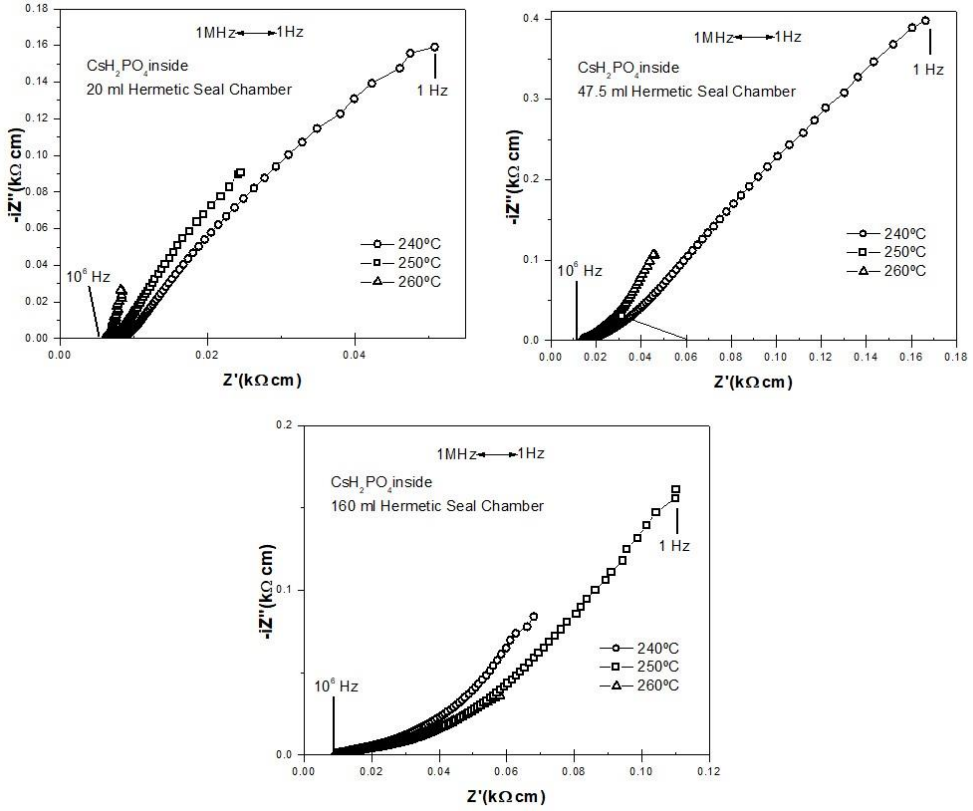

Figure 4.11 Nyquist plots of CsH_2PO_4 using 20ml, 47.5ml and 160ml hermetically sealed chambers at temperatures above T_{SP}.

Figure 4.12 displays the effect on the proton conductivity of the CsH_2PO_4 over a range of temperatures when it is measure using the different volume hermetically sealed chambers, 50ml vacuum pulling out vacuum and without a chamber, as a reference. At T= 200ºC, the 160ml chamber (diamonds) have the highest proton conductivity with ~1.3×10^{-5}S·cm^{-1}, followed very close by the 20ml chamber (squares) with ~1.1×10^{-5}S·cm^{-1} and the lowest value for the proton conductivity is the sample under vacuum with ~3.2×10^{-6}S·cm^{-1}. The dataset indicates that by using a smaller volume contained chamber, even under vacuum, helps to increase the proton conductivity of CsH_2PO_4 at temperatures above T_{SP}, rather than having the sample measure without a chamber.

At 260ºC the 20ml chamber (squares) have the best performance with ~3×10^{-2}S·cm^{-1}, followed by the 160ml Chamber (diamonds) ~2×10^{-2}S·cm^{-1} and the sample measured without a chamber (circles) have the lowest performance with ~3.6×10^{-3}S·cm^{-1}.

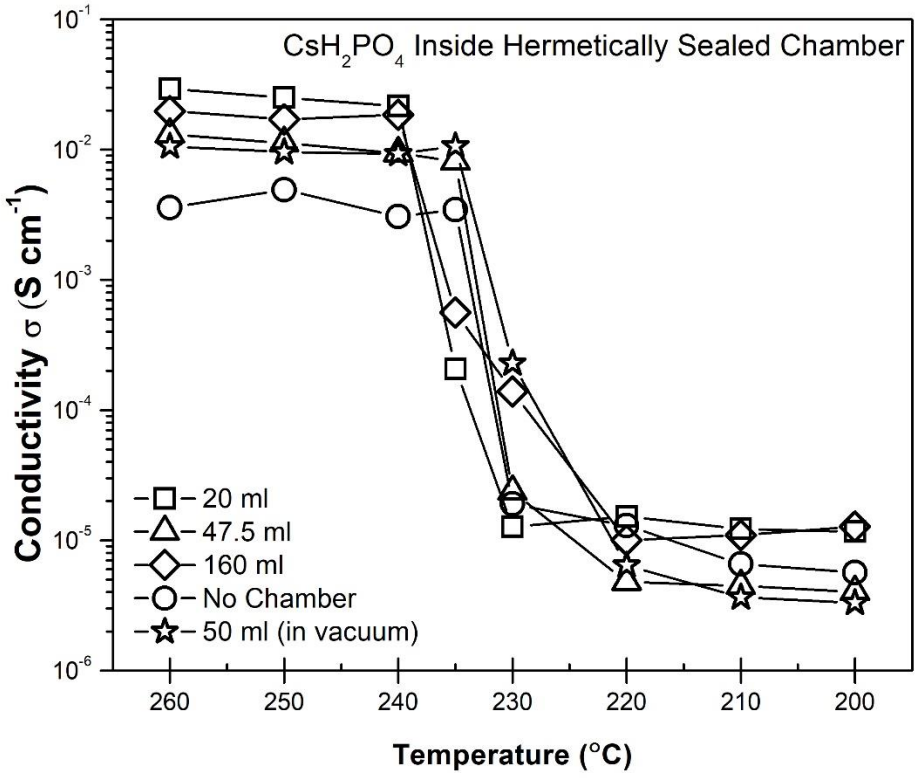

Figure 4.12 Temperature resolved proton conductivity for CsH_2PO_4 by using different chambers and without a chamber

4.6. STABILITY OF SUPERPROTONIC CONDUCTIVITY OF CsH_2PO_4 BY THE USAGE OF HERMETICALLY SEALED CHAMBERS AND UNDER VACUUM

To study the stability of CsH_2PO_4 in each of the hermetically sealed chambers and under vacuum, we ran a 10 hours isotherm study (at 260ºC) of the proton conductivity of neat CsH_2PO_4. The results of neat CsH_2PO_4 under air (~20%rh) from section 3.2 was used as a reference.

Figure 4.13 provides a clear trend in the proton conductivity *vs.* time dependence; when CsH_2PO_4 is under the 20ml chamber (squares), it offers the heights values for proton conductivity ($\sim 3\times10^{-2} S\cdot cm^{-1}$) and its very stable, remaining constant for the whole timespan of the study. The second-best performance was display by the 47.5ml chamber (triangles) presenting a conductivity of $\sim 3\times10^{-2}\ S\cdot cm^{-1}$ and with a constant value as well for the 10 hours. Clearly, increasing the volume size of the chambers had an effect for the stability of the sample, the sample on the 160ml chamber (diamonds) started to decay its value even at the first hour of the experiment, and started to stabilize after the third hour, but with a lower proton conductivity of $\sim 1.9\times10^{-2} S\cdot cm^{-1}$. When compared with the CsH_2PO_4 under air, in which the sample is contain in a much larger volume, it's clear that the sample presents a better performance contained inside a smaller chamber.

Finally, when the sample was run under vacuum (stars), it rapidly started to decrease its proton conductivity and is not stable at all. Is evident that the pressure that the air inside the hermetically sealed chamber provides to the sample helps the stabilization of superprotonic phase of CsH_2PO_4 even without humidity around it.

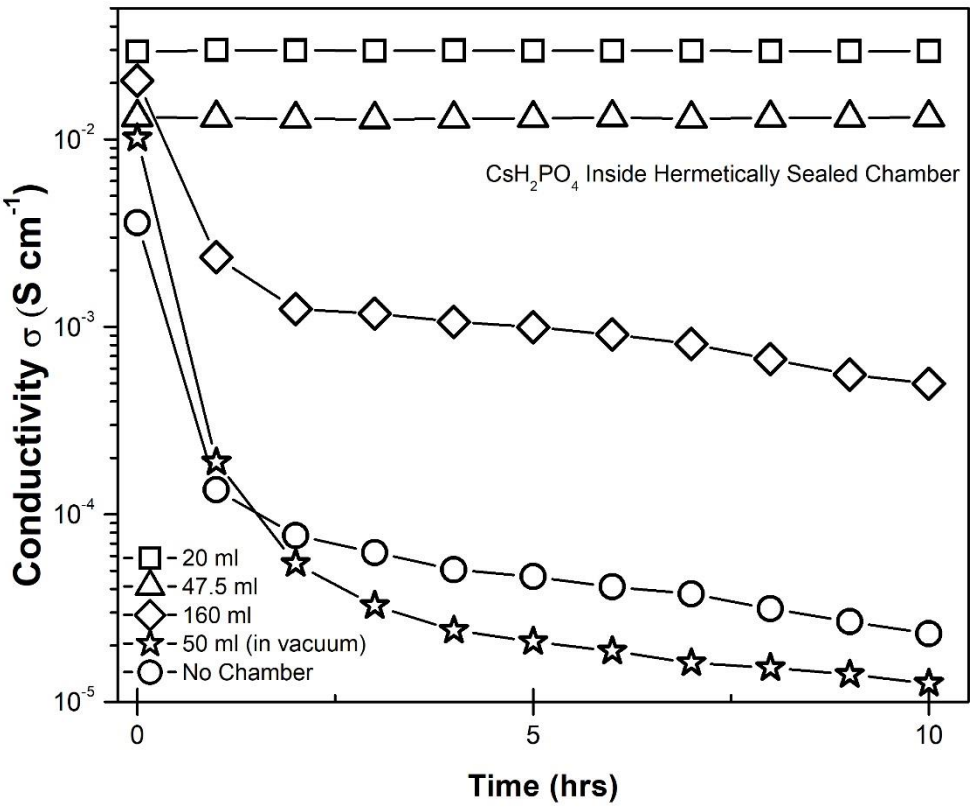

Figure 4.13 Isotherms (260ºC) of proton conductivity time study for CsH_2PO_4 by using different chambers and without a chamber

4.7. EFFECT OF THE USAGE OF DIFFERENT GASES IN A 20-ML HERMETICALLY SEALED CHAMBER ON THE SUPERPROTONIC CONDUCTION OF CsH_2PO_4

Motivated by the results of the proton conductivity using a 20ml hermetically sealed chamber, we designed another hermetically sealed gas chamber (with the same volume to be consistent) that have ability to flow gas inside it. An Impedance Spectroscopy study using the same parameters as the other two experiments, to keep consistency, was executed. Using a "T" connection, one line was connected to a tank that provided a specific gas, meanwhile another goes to the chamber and a third one to a vacuum pump. Through the use of valves, a pump and flush

procedure was performed to the chamber three times before the experiment began to fully replace the air inside the chamber with other gas. The set up for this procedure is shown in illustration 4.3. One Line is connected to the gas tank, another to the chamber and a third line goes to a vacuum pump. The gas chamber was fill independently with Argon, Helium, air, Nitrogen or dry air (with no humidity). The results obtained without the chamber were used as a reference.

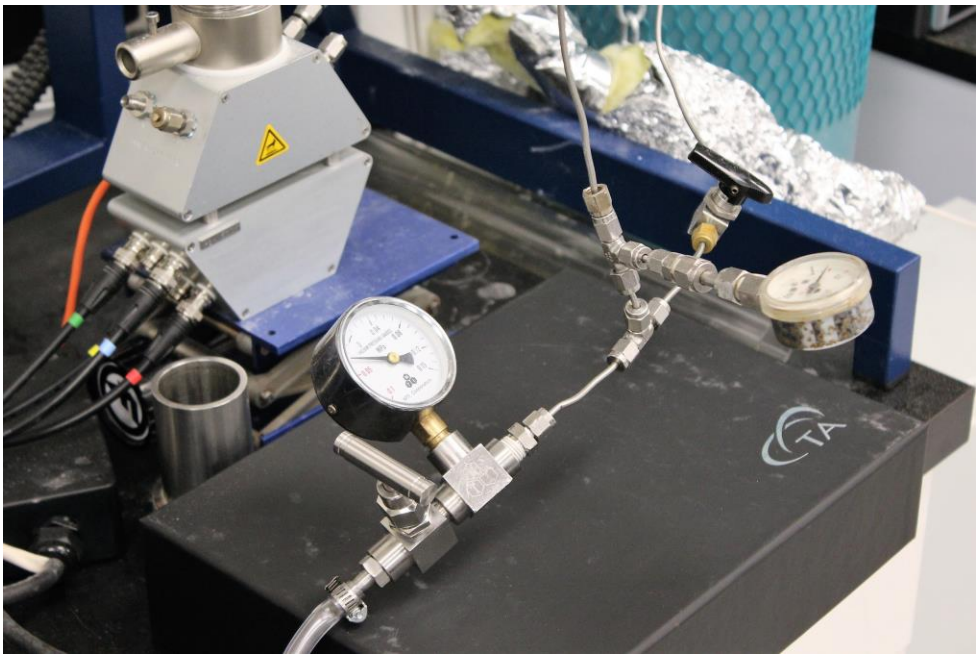

Illustration 4.3 Setup used to replace ambient air (~20%rh) with another gas inside the chamber.

Figure 4.14 present the Nyquist plots of the sample measured at temperatures below T_{SP}, T=200ºC (triangles), T=210ºC (circles) and T=220ºC (rectangles) for each gas used to fill the hermetically sealed chamber and under vacuum. Each gas at all temperatures, the semicircles intersect the real axis of the impedance at a frequency of 10^3Hz and later we calculated the proton conductivity.

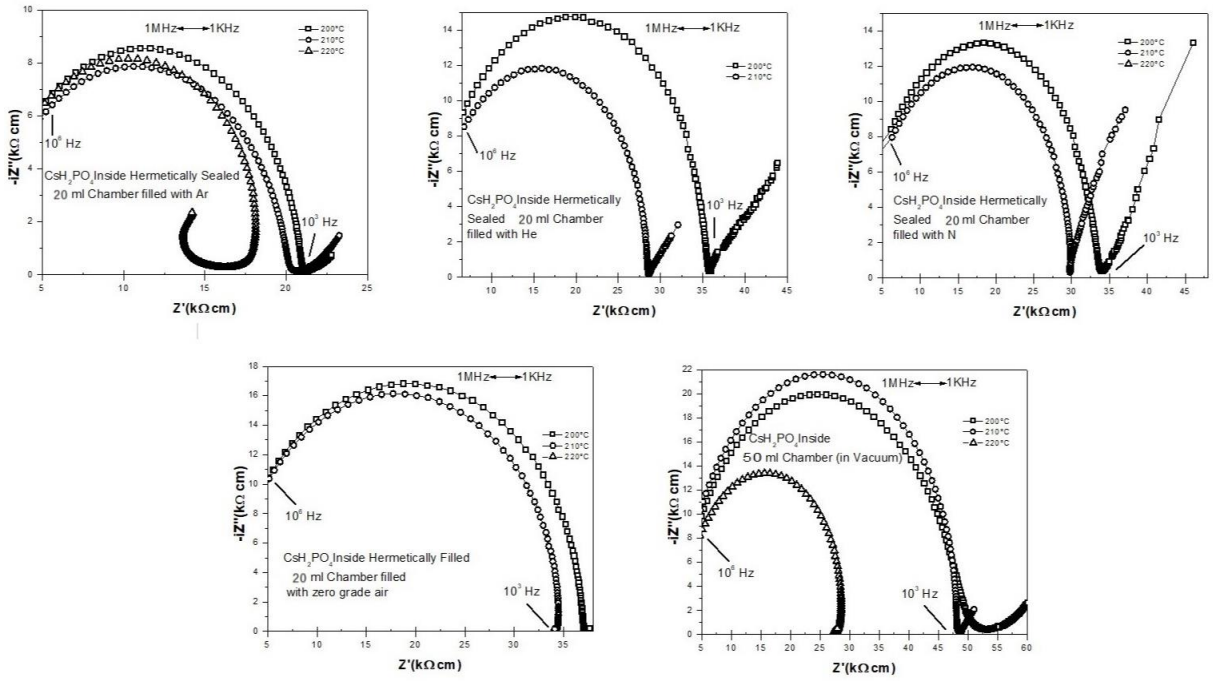

Figure 4.14 Nyquist plots for each gas used to fill the hermetically sealed 20ml chamber at temperatures below T_{SP}

Now, figure 4.15 focuses on the Nyquist plots at temperatures above T_{SP}, T=240°C (triangles), T=250°C (circles) and T=260°C (rectangles) for each gas used. The samples reach surperprotonic phase, In the Nyquist plots small semicircles can been seeing at high frequencies along with a predominant linear, characteristic of the superprotonic phase.

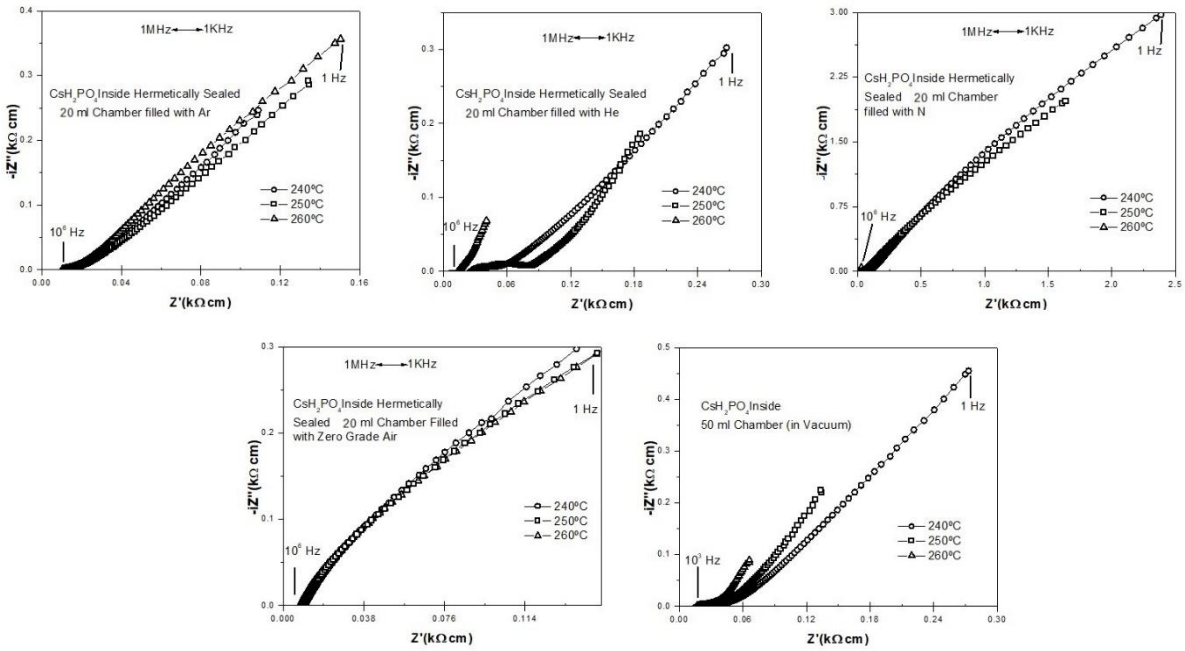

Figure 4.15 Nyquist plots for each gas used to fill the hermetically sealed 20ml chamber at temperatures above T_{SP}

Figure 4.16 show how the sample's proton conductivity changes over a temperature range of 200ºC to 260ºC, for each of the gases used. CsH_2PO_4 measured in dry conditions and using the hermetically sealed chamber filled with air, as in the study 3.5 were used as a reference. A very noticeable change in this study is that when using Argon (Squares), the jump to super protonic phase started at 220ºC, whereas with Helium (triangles), Nitrogen (diamonds) and even with the zero-grade air (star) the transition started to happen at 210ºC. This shows that the transition into the super protonic phase starts at lower temperatures than when it was at dry conditions of using air inside the chamber that started at 235ºC. The proton conductivity for each gas after T_{SP} are very close to each other. At T= 260ºC the values for Argon ~$1.9\times10^{-2}S\cdot cm^{-1}$, Helium ~$1.4\times10^{-2}S\cdot cm^{-1}$, Nitrogen ~$1.7\times10^{-2}S\cdot cm^{-1}$, zero grade air ~ $2.3\times10^{-2}S\cdot cm^{-1}$. On the other hand, as previously reported in 3.2, for air $\sigma \sim 2.9\times10^{-2}S\cdot cm^{-1}$ and without using the hermetically sealed chamber $\sigma \sim 3.6\times10^{-3}S\cdot cm^{-1}$.

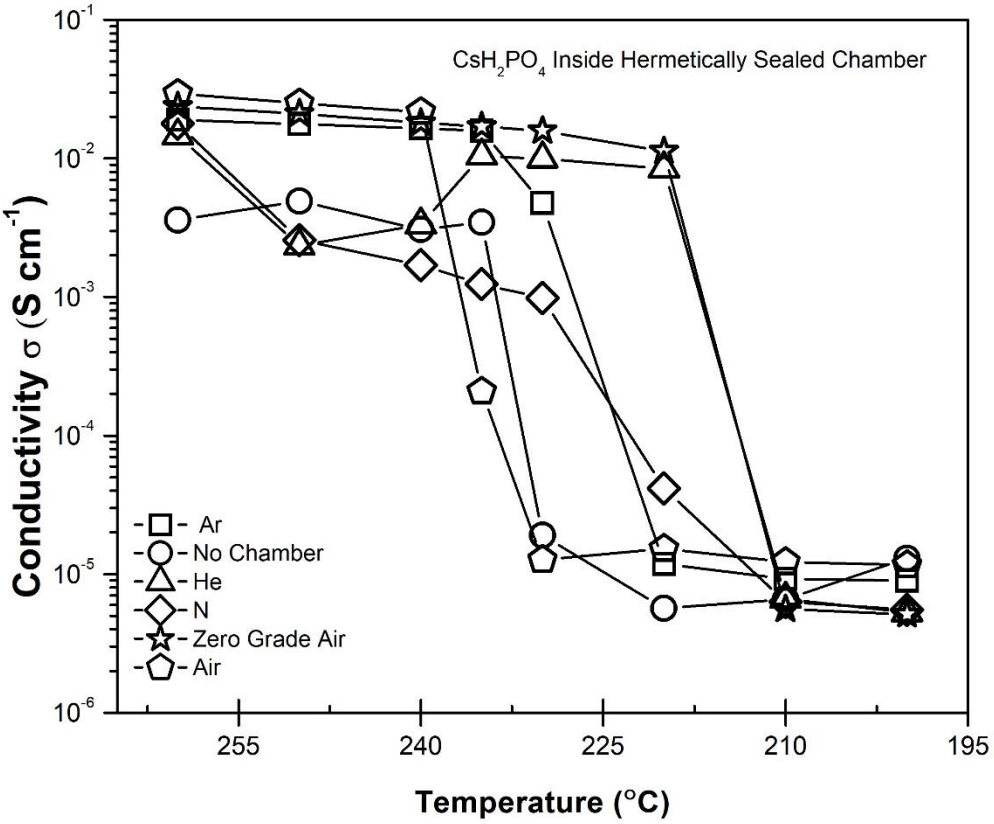

Figure 4.16 Temperature resolved proton conductivity for CsH_2PO_4 by using different gases inside hermetically sealed 20ml chamber

4.8. STABILITY OF SUPERPROTONIC CONDUCTIVITY OF CsH_2PO_4 BY THE USAGE OF A 20 ML HERMETICALLY SEALED CHAMBER FILLED WITH DIFFERENT GASES AND UNDER VACUUM

In the final part of our study, we carried out a 10 hours isotherm study (at 260°C) of the proton conductivity of neat CsH_2PO_4 using the hermetically sealed 20ml chamber filled out independently with Argon, Helium, air, Nitrogen or dry air (with no humidity). The results obtained without the chamber were used as a reference.

Figure 4.17 uncovers the proton conductivity *vs.* time dependence measured on neat CsH_2PO_4 under different gases, under vacuum and without a chamber. It's clear, with the exception of Helium, that the use of any gas inside the hermetically sealed chamber helps the CDP to have a solid performance over a 10h timespan. When air is used inside the chamber have its highest

protonic conductivity $\sigma \sim 3\times10^{-2}S\cdot cm^{-1}$and this value remains unchanged through the 10 hours. When zero grade air is used, a protonic conductivity of $\sigma \sim 2.3\times10^{-2}S\cdot cm^{-1}$ it's exhibited. As mentioned before, when helium it's employed, after the 4th hour its protonic conductivity starts to rapidly decrease. However, not surprisingly, when the sample its run without the chamber it's that have its worst performance, and even after its second hour of use, its proton conductivity rapidly decreases. Going from $\sim 3.6\times10^{-3}S\cdot cm^{-1}$ at the start of the study to $\sim 1.3\times10^{-4}S\cdot cm^{-1}$ at its second hour to finally $\sim 2.3\times10^{-2}S\cdot cm^{-5}$ after 10 hours.

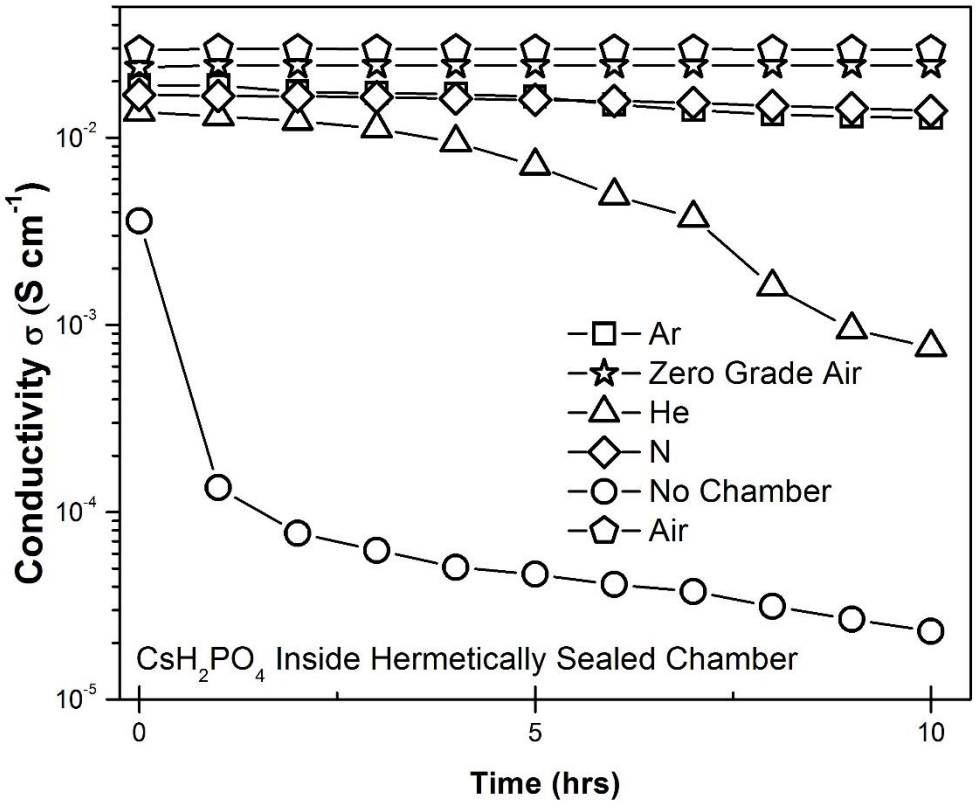

Figure 4.17 Isotherms (260ºC) of proton conductivity time study for CsH_2PO_4 inside hermetically sealed chamber filled out independently with different gases and without a chamber

Chapter 5: Conclusions

Through a temperature resolve XRD study we identified the microstructural details of the polymorphic transition on CsH_2PO_4 from monoclinic ($P2_1/m$) to cubic (Pm-3m) that is associated with the superprotonic conductivity. This was later supported by the DSC measurements that identify endotherms on CsH_2PO_4 around T_{SP} at ~232^oC, which coincides with the jump in protonic conductivity of the sample.

The Impedance Spectroscopy study performed on CsH_2PO_4 in air reported a three-order-of-magnitude proton conductivity jump in CsH_2PO_4 around T_{SP}. When an isotherm (at 260^oC) impedance spectroscopy study for 10 hours was performed under air (~20%rh) and humid environment (P_{H2O} ~ 0.38atm.), the sample under a humid environment exhibited a more stable performance than its contra part.

When CsH_2PO_4 was mechanically mixed with nano-silica, forming the compounds of (1-x)CsH_2PO_4 / xSiO_2 ($0<x<.3$), both present higher values proton conductivity for x=0.2 before and after T_{SP} and are more stable over 10 hours run in air, than the unmixed sample. However, having the sample under a humid environment outperforms any sample in dry environment.

The use of hermetically sealed chambers of different volumes and filled out independently with several nonreactive gases and under vacuum to measure the proton conductivity of CsH_2PO_4 provided a better insight on the proton conductivity performance. Using the smallest volume chamber of 20ml and filled with zero grade air have a better performance than the other set ups. Further studies are required to determine the cause of this behavior, but it could be attributed than zero grade air it's already saturated and keep the water of CsH_2PO_4 within the pellet, delaying the dehydration of the sample.

References

[1] I. A. Stenina, E. Y. Safronova, A. V. Levchenko, Y. A. Dobrovolsky, and A. B. Yaroslavtsev, "Low-temperature fuel cells: Outlook for application in energy storage systems and materials for their development," *Therm. Eng.*, vol. 63, no. 6, pp. 385–398, 2016.

[2] I. A. Stenina and A. B. Yaroslavtsev, "Low- and intermediate-temperature proton-conducting electrolytes," *Inorg. Mater.*, vol. 53, no. 3, pp. 253–262, 2017.

[3] D. S. Scott and W. Häfele, "The coming hydrogen age: Preventing world climatic disruption," *Int. J. Hydrogen Energy*, 1990.

[4] H. Tang, Z. Wan, M. Pan, and S. P. Jiang, "Self-assembled Nafion-silica nanoparticles for elevated-high temperature polymer electrolyte membrane fuel cells," *Electrochem. commun.*, 2007.

[5] O. Z. Sharaf and M. F. Orhan, "An overview of fuel cell technology: Fundamentals and applications," *Renewable and Sustainable Energy Reviews*. 2014.

[6] K. Sopian and W. R. Wan Daud, "Challenges and future developments in proton exchange membrane fuel cells," *Renew. Energy*, vol. 31, no. 5, pp. 719–727, 2006.

[7] "Fuel cell technology," 2009. [Online]. Available: http://ac.umicore.com/en/applications/fuel-cell-catalysts/.

[8] F. Samimi and Mohammad R.Rahimpour, *Methanol: Science and Engineering*. 2018.

[9] O. Paschos, J. Kunze, U. Stimming, and F. Maglia, "A review on phosphate based, solid state, protonic conductors for intermediate temperature fuel cells," *J. Phys. Condens. Matter*, vol. 23, no. 23, 2011.

[10] S. P. S. Badwal, S. Giddey, C. Munnings, and A. Kulkarni, "Review of progress in high temperature solid oxide fuel cells," *J. Aust. Ceram. Soc.*, 2014.

[11] K. Scott, C. Xu, and X. Wu, "Intermediate temperature proton-conducting membrane electrolytes for fuel cells," *Wiley Interdiscip. Rev. Energy Environ.*, vol. 3, no. 1, pp. 24–41, 2014.

[12] A. I. Baranov, V. V. Grebenev, A. N. Khodan, V. V. Dolbinina, and E. P. Efremova, "Optimization of superprotonic acid salts for fuel cell applications," *Solid State Ionics*, 2005.

[13] a I. Baranov, L. a Shuvalov, and N. M. Shchagina, "Superion conductivity and phase transitions in CsHSO4 and CsHSeO4 crystals," *JETP lett*, vol. 36, no. 11. pp. 459–462, 1982.

[14] A. I. Baranov, B. V. Merinov, A. V. Tregubchenko, V. P. Khiznichenko, L. A. Shuvalov, and N. M. Schagina, "Fast proton transport in crystals with a dynamically disordered hydrogen bond network," *Solid State Ionics*, 1989.

[15] C. E. Botez *et al.*, "High-temperature phase transitions in CsH2PO4 under ambient and high-pressure conditions: A synchrotron x-ray diffraction study," *J. Chem. Phys.*, vol. 127, no. 19, p. 194701, 2007.

[16] S. M. Haile, D. A. Boysen, C. R. I. Chisholm, and R. B. Merie, “Solid acids as fuel cell electrolytes,” *Nature*, 2001.

[17] R. B. Merle, C. R. I. Chisholm, D. A. Boysen, and S. M. Haile, “Instability of sulfate and selenate solid acids in fuel cell environments,” *Energy and Fuels*, 2003.

[18] D. A. Boysen, T. Uda, C. R. I. Chisholm, and S. M. Haile, “High-Performance Solid Acid Fuel Cells Through Humidity Stabilization,” *Science (80-.).*, 2004.

[19] J. Otomo *et al.*, “Effect of water vapor on proton conduction of cesium dihydrogen phosphate and application to intermediate temperature fuel cells,” pp. 865–870, 2005.

[20] C. E. Botez *et al.*, “High-temperature phase transitions in CsH2PO4 under ambient and high-pressure conditions: A synchrotron x-ray diffraction study,” *J. Chem. Phys.*, 2007.

[21] B. Pejcic and R. De Marco, “Impedance spectroscopy: Over 35 years of electrochemical sensor optimization,” *Electrochimica Acta*. 2006.

[22] D. V. Ribeiro and J. C. C. Abrantes, “Application of electrochemical impedance spectroscopy (EIS) to monitor the corrosion of reinforced concrete: A new approach,” *Constr. Build. Mater.*, 2016.

[23] D. D. MacDonald, “Reflections on the history of electrochemical impedance spectroscopy,” in *Electrochimica Acta*, 2006.

[24] Princeton Applied Research, “Basics of Electrochemical Impedance Spectroscopy,” *Application Note AC*, 2008.

[25] B. A. Mei, O. Munteshari, J. Lau, B. Dunn, and L. Pilon, “Physical Interpretations of Nyquist Plots for EDLC Electrodes and Devices,” *J. Phys. Chem. C*, 2018.

[26] S. M. Haile, C. R. I. Chisholm, K. Sasaki, D. A. Boysen, and T. Uda, “Solid acid proton conductors: from laboratory curiosities to fuel cell electrolytes,” *Faraday Discuss.*, vol. 134, pp. 17–39, 2007.

[27] C. Kittel, “Introduction to solid state physics,” *Solid State Phys.*, 2005.

[28] Kittel, C. Kittel, Charles Kittel, and C. Kittel, *Introduction to Solid State Physics, 8th Edition*. 2010.

[29] B. D. Cullity, “Elements of X-ray diffraction, 2nd edition,” *Addison-Wesley Publ. Co. Read. MA*, 1978.

[30] Https://www.fhi-berlin.mpg.de/~wolf/femtoweb/teaching/WS0506-wolf-festk/WS0506/material/diffraction3_4.pdf, “No Title.” [Online]. Available: https://www.fhi-berlin.mpg.de/~wolf/femtoweb/teaching/WS0506-wolf-festk/WS0506/material/diffraction3_4.pdf.

[31] A. I. Baranov, V. P. Khiznichenko, V. A. Sandur, and L. A. Shuvalov, “Frequency Dielectric Dispersion In The Ferroelectric And Superionic Phases Of Csh2 Po4,” *Ferroelectrics*, 1988.

[32] S. M. Haile, C. R. I. Chisholm, K. Sasaki, D. A. Boysen, and T. Uda, “Solid acid proton conductors: From laboratory curiosities to fuel cell electrolytes,” in *Faraday Discussions*, 2007.

[33] A. Chauhan, “Powder XRD Technique and its Applications in Science and Technology,” *J. Anal. Bioanal. Tech.*, 2014.

[34] “http://www.xtal.iqfr.csic.es/Cristalografia/parte_05_5-en.html.” .

[35] “https://de.wikipedia.org/wiki/Debye-Scherrer-Verfahren.” .

[36] L. Van Vu, S. C. Doanh, L. T. Nga, and N. N. Long, “Properties of PbS Nanocrystals Synthesized by Sonochemical and Sonoelectrochemical Methods,” *e-Journal Surf. Sci. Nanotechnol.*, 2011.

[37] J.-H. Park, “Possible origin of the proton conduction mechanism of CsH2PO4 crystals at high temperatures,” *Phys. Rev. B*, 2004.

[38] A. I. Baranov, V. P. Khiznichenko, and L. A. Shuvalov, “High Temperature Phase Transitions And Proton Conductivity In Some Kdp-Family Crystals,” *Ferroelectrics*, 1989.

[39] W. Bronowska, “Comment on ‘Does the structural superionic phase transition at 231°C in CsH2PO4really not exist?’ [J. Chem. Phys. 110, 4847 (1999)],” *Journal of Chemical Physics*. 2001.

[40] V. G. Ponomareva and E. S. Shutova, “High-temperature behavior of CsH2PO4 and CsH2PO4-SiO2 composites,” *Solid State Ionics*, 2007.

[41] J. Otomo, T. Ishigooka, T. Kitano, H. Takahashi, and H. Nagamoto, “Phase transition and proton transport characteristics in CsH2PO4/SiO2 composites,” *Electrochim. Acta*, 2008.

[42] G. Kim, J. M. Griffin, F. Blanc, S. M. Haile, and C. P. Grey, “Characterization of the dynamics in the protonic conductor CsH<inf>2</inf>PO<inf>4</inf> by ^{17}O solid-state NMR spectroscopy and first-principles calculations: Correlating phosphate and protonic motion,” *J. Am. Chem. Soc.*, 2015.

[43] A. Ikeda and S. M. Haile, “The thermodynamics and kinetics of the dehydration of CsH2PO4studied in the presence of SiO2,” in *Solid State Ionics*, 2012.

[44] D. A. Boysen, S. M. Haile, H. Liu, and R. A. Secco, “High-temperature behavior of CsH<inf>2</inf>PO<inf>4</inf> under both ambient and high pressure conditions,” *Chem. Mater.*, 2003.

[45] J. Otomo, N. Minagawa, C. J. Wen, K. Eguchi, and H. Takahashi, “Protonic conduction of CsH2PO4and its composite with silica in dry and humid atmospheres,” *Solid State Ionics*, 2003.

[46] E. Ortiz, R. A. Vargas, and B. E. Mellander, “On the high-temperature phase transitions of CsH2PO4: A polymorphic transition? A transition to a superprotonic conducting phase?,” *J. Chem. Phys.*, 1999.

[47] E. Ortiz, R. A. Vargas, and B. E. Mellander, “On the high-temperature phase transitions of some KDP-family compounds: A structural phase transition? A transition to a bulk-high proton conducting phase?,” *Solid State Ionics*, 1999.

Vita

Israel Martinez Vital was born and raised in Mexico City Juarez, Mexico in December 18th, 1979. He earned his Bachelor of Science degree in Physics Engineering from The Universidad Autónoma de Ciudad Juárez in 2003. In 2006, he received his Master of Science degree in Physics from The University of Texas at El Paso. In 2013, he joined the Doctoral Program of Materials Science and Engineering at The University of Texas at El Paso.

Israel Martinez Vital was awarded a scholarship from the Consejo Nacional de Ciencia y Tecnologia (CONACyT) from his native country, Mexico, which supported his doctoral studies.

From 2007 to 2008 Israel Martinez taught high school and college level course at the Instituto Tecnológico de Estudios Superiores de Monterrey in Ciudad Juarez, Mexico. Also, from 2007 to 2015 he taught Physics college level courses at his alma mater.

From 2009 to 2015 he worked as a Research and Development engineer for OSRAM Sylvania. While pursuing his degree, Israel Martinez Vital worked as a research assistant for Dr. Botez during his doctoral studies.

He presented his research at regional meetings of the American Physical Society at Las Cruces, NM, and Dallas, TX, at the Graduate Research Expo at The University of Texas at El Paso, at the American Crystallographic Association at Denver, Colorado; at theTexas Academy of Science at Midland Texas and finally at the First CONACyT Grant Holders Meeting in North America at Washington D.C. His current publication is titled "Stability of the superprotonic conduction of (1-x)CsH2PO4/xSiO2 ($0 \leq x \leq 0.3$) composites under dry and humid environments".

Israel Martinez Vital was actively involved in the Society for Biomaterials, UTEP Chapter as the Treasurer from 2016-2018.

E-mail address: imartinez6@miners.utep.edu

This dissertation was typed by Israel Martinez Vital